Sleep-modulated disinhibition enables replay for memory consolidation, accelerated by ripples

Shrey Dutta [1*]

1 Independent researcher, Sahiya, Uttarakhand, India

* shreyndutta@gmail.com

Abstract

Memory consolidation involves elusive neural mechanisms. Here, we develop a biophysically detailed model of the entorhinal-hippocampal-cortical network to reveal that disinhibition drives synaptic and systems consolidation. Transitioning to slow-wave sleep via neuromodulatory dampening of inhibition generates up-down states and spontaneous, time-compressed replays of spatial sequences encoded with theta-phase precession. Lateral inhibition levels unify physiological and pathological ripple diversity. Cortical disinhibition enables memory transfer from hippocampus. Weakened afferent CA1 synapses eliminate ripples but spare replays, proposing strategies to mitigate ripple disruptions. Replays sustain systems consolidation even without ripples, albeit slower; excessive weakening halts it, rescuable by enhanced hippocampal-to-cortical connectivity. Inducing disinhibition during wakefulness—mimicking medial-entorhinal-cortex-input-dependent quiet wakefulness replay—activates these processes, underscoring disinhibition's state-agnostic role. These insights elucidate disinhibition's centrality in engraining memories and fostering hippocampal independence, reconciling empirical observations, yielding testable predictions, and identifying therapeutic avenues for memory disorders.

Introduction

Memory consolidation, the process that transforms transient experiences into enduring memories, is fundamental to learning and cognition [1–5]. It encompasses synaptic consolidation—stabilizing memory engrams locally in the hippocampus [6–10]—and systems consolidation—integrating engrams with cortical networks [11–15]. Both rely on neural phenomena during slow-wave sleep [16–21] and quiet wakefulness [22–25]: memory replays reactivating sequential neural patterns from recent experiences [26–32]; sharp-wave ripples (SWRs), high-frequency oscillations that synchronize neuronal firing to promote synaptic plasticity [3, 33, 34]; and replay-mediated transfer redistributing hippocampal engrams to cortical regions (e.g., retrosplenial or prefrontal cortex), enabling long-term storage independent of the hippocampus [35–39]. Despite significant progress, the mechanisms initiating and regulating these phenomena remain elusive.

Emerging evidence reshapes our understanding of hippocampal SWR generation, focusing on disinhibition regulated by neuronal and neuromodulatory factors [40–42].

Traditionally, SWRs were thought to initiate sequential replay activity [43, 44]—but ripple-less replays [45] indicate independent mechanisms that remain to be elucidated. Moreover, although transient cortical disinhibition is necessary for hippocampal-to-cortical communication [46, 47], concurrent sleep-state alterations in inhibitory circuits [48–56] challenge its sufficiency, necessitating a refined mechanistic framework.

Studies indicate that SWRs facilitate hippocampal-to-cortical transfer of replayed sequences, as evidenced by co-occurrence with hippocampal replays [57–62] and ensuing cortical activity [63–66], along with impaired memory recall following ripple-associated replay disruption [67–72]. Wakeful ripple-associated replays tag engrams for selective sleep consolidation [73]. Ripple-less replay of non-salient trajectories [45] refines this view, since trajectory saliency dictates ripple coupling and thereby replay prioritization for cortical storage [74, 75]. These insights prompt pivotal questions: What mechanistic distinctions underlie ripple-associated versus ripple-less replay? Can ripple-less replay mediate hippocampal-to-cortical engram transfer?

To address these questions, existing models often omit biophysical integrations critical for multi-region dynamics across sleep-wake states. We thus develop a computational model of the entorhinal-hippocampal-cortical network, incorporating Hodgkin-Huxley neurons [76]; synaptic plasticity rules [77] including dynamic feedforward [78], feedback and lateral inhibition [79]; short-term plasticity [80]; inter- and intra-regional delays [81]; theta-phase precession during encoding [82]; protein-mediated synaptic stabilization [83]; spine addition/removal [84]; and ionic dynamics for awake-sleep transitions [85]. This model simulates stimulus-triggered sequence encoding, spontaneous hippocampal replay and SWRs upon slow-wave sleep onset, and both synaptic and systems-level memory consolidation.

Results

Medial entorhinal cortex stimulation drives entorhinal-hippocampal spatial memory encoding

Our model includes neuronal populations for the medial entorhinal cortex (MEC), hippocampal subregions (dentate gyrus, DG; CA3; CA1), cortical regions (CR, e.g., prefrontal or retrosplenial cortex), and a background population that simulates asynchronous-irregular synaptic inputs during wakefulness [86, 87] and up-down dynamics during slow-wave sleep (SWS) [88] from unmodeled brain regions (Fig. 1a,b; Methods). To simulate the wakefulness-to-SWS transition, we lowered extracellular potassium buffer concentration ($[K^+]_{\text{Buffer}}$) from 3.5 to 3.0 mM, reflecting the observed drop in extracellular potassium concentration ($[K^+]_o$) during natural sleep [85]. This $[K^+]_o$ reduction decreases neuronal excitability via hyperpolarized resting potentials [85] and weakens inhibitory synaptic efficacy [48] via a K^+-dependent disinhibition modulating factor (Methods), inducing SWS-typical up-down dynamics (Fig. 1b) [89].

Excitatory-to-excitatory synaptic strengths evolve via triplet-spike-timing-dependent plasticity (triplet-STDP) [77], with proportional adjustments to associated inhibitory

synapses for balanced feedforward, feedback, and lateral inhibition (Fig. 1a; Methods). Spatial navigation was simulated by sequentially stimulating location-specific MEC excitatory assemblies with theta-phase-precessing spike bursts (Fig. 1c; Methods) [82]. Efferent MEC projections elicited delayed activation of corresponding assemblies in DG, CA3, and CA1, driving synaptic potentiation across regions (Fig. 1d) [90]. This strengthened initially weak MEC→MEC, DG→CA3, and CA3→CA3 synapses to encode sequence A–D, while enhancing MEC→DG/CA3/CA1 and CA3→CA1 projections. Strong CA1→CR feedforward inhibition [91–94] (Methods) limited CR activity below potentiation thresholds and thereby induced synaptic depression during exploration [95], preventing premature sequence maturation and allowing cortical engram recall only post-offline consolidation [37]. Potentiation saturates at peak spine receptor density but remains labile until protein-mediated synaptic stabilization (Methods).

Potentiated synapses stabilize over hours through lingering plasticity-related proteins (PRPs) from encoding, independent of engram reactivation [96]. To save stabilization time before sleep simulations, we assumed complete stabilization of encoding-induced changes by equating stable synaptic weights ($\widetilde{w}$) to overall (stable+labile) weights (w) and resetting PRPs to zero, enabling new spine formation and further potentiation during offline reactivation (Methods).

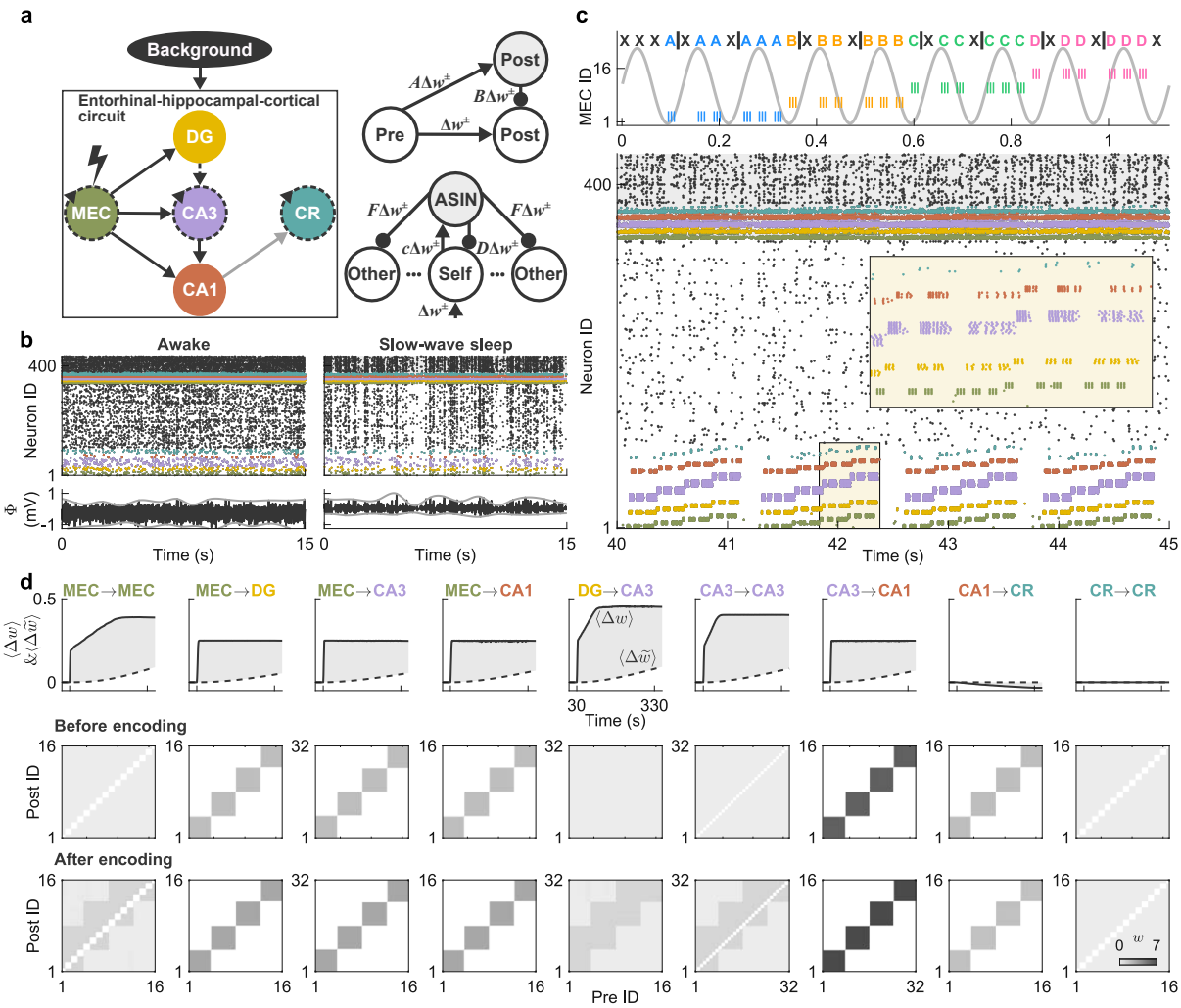

Fig 1: Entorhinal-hippocampal-cortical circuit model, awake/sleep dynamics, and stimulation-driven encoding. **a** Left: Schematic of the entorhinal-hippocampal-cortical circuit driven by background neural activity. Brain regions: medial entorhinal cortex (MEC, green), dentate gyrus (DG, yellow), CA3 (purple), CA1 (red), cortical regions (CR, blue-green), unmodeled brain regions (Background, black). Black solid arrows denote effective pre-encoding connections (MEC→DG, MEC→CA3, MEC→CA1, CA3→CA1). Gray solid arrow (CA1→CR) indicates anatomical connection with strong feedforward inhibition during wakefulness. Dashed arrows show ineffective (weak) pre-encoding connections (DG→CA3; recurrent in MEC, CA3, CR). Lightning bolt on MEC signifies stimulation initiating encoding. Right top: Dynamic synaptic updates for feedforward inhibition. Neurons: presynaptic excitatory ('pre', unfilled circle), postsynaptic excitatory ('post', unfilled circle) or inhibitory (gray filled circle). Updates: $\Delta w^{\pm}$ from 'pre' to excitatory 'post' drives $A\Delta w^{\pm}$ to 'pre'→inhibitory 'post' and $B\Delta w^{\pm}$ to inhibitory 'post'→excitatory 'post', where $A = a/M$, $B = b/M$, M is the number of interneurons in the feedforward inhibition path from 'pre' to 'post', and a, b are scaling constants. Right bottom: Dynamic synaptic updates for feedback and lateral inhibition. Neurons: excitatory in the assembly of 'post' ('self', middle unfilled circle), in other assemblies ('other', left/right unfilled circles), assembly-specific inhibitory neuron (ASIN, filled circle). Updates: $\Delta w^{\pm}$ to 'post' drives $c\Delta w^{\pm}$ to 'post'→ASIN, $D\Delta w^{\pm}$ to ASIN→'self' (feedback), $F\Delta w^{\pm}$ to ASIN→'other' (lateral), where $D = d/N$, $F = f/N$, N is the number of neurons in the assembly, and c, d, f are scaling constants. Arrows: excitatory; round arrowheads: inhibitory. **b** Extracellular potassium buffer ($[K^+]_{\text{Buffer}}$) decrease (3.5 to 3.0 mM) transitions the dynamics from 'awake' to 'slow-wave sleep' via disinhibition. Top: Raster plots of spikes from 435 neurons (1–336 excitatory, 337–435 inhibitory) showing 'awake' (asynchronous-irregular; left) and 'slow-wave sleep' (up-down; right) dynamics before encoding. Bottom: Respective local field potential activity, (Φ), from 'Background' neurons. Gray lines trace the upper and lower envelopes. **c** Top: Stimulation pattern mimicking exploration from locations A to D with theta-phase precession for 16 MEC neurons over 1.125 s. Each gray 8 Hz theta cycle (9 cycles, 125 ms each) is organized into four phases, with colored letters (blue A, orange B, green C, pink D: locations; black X: none) marking burst stimulation (three spikes) in the four neurons of each location-specific cell assembly, advancing to earlier phases with successive cycles. Bottom: Raster plot over 5 s during four complete stimulations of locations (MEC cell assemblies in green) 'A' to 'D'. Inhibitory neurons at top with gray shading. Background activity (black) is asynchronous irregular ('awake'). MEC stimulation drives downstream activity via effective connections (panel **a**). Inset: Zoomed view of the latter part of the second stimulation (boxed), showing delayed activation in downstream regions for locations C and D. **d** Top: Time course of changes (Δ) in mean excitatory-to-excitatory synaptic weights for connections in panel **a** during stimulation-driven encoding ($\langle\Delta w\rangle$, solid: fast overall [labile + stable] governed by spike-timing-dependent plasticity; $\langle\Delta\widetilde{w}\rangle$, dashed: slow stable governed by protein-mediated stabilization; $\langle\Delta w\rangle - \langle\Delta\widetilde{w}\rangle$, shading: labile component). The 5-min stimulation period (from 30 s to 330 s) represents repeated sequential exploration of locations 'A' to 'D'. Middle & bottom: Matrices showing overall weights, w, between neurons before (middle) and after (bottom) the stimulation-driven encoding; white indicates no connection.

Hippocampal disinhibition enables sequential replay of encoded engrams via inter-assembly delay

Following encoding, we transitioned to SWS dynamics. Reduced feedforward inhibition via a K^+-dependent disinhibition factor (Methods) triggered spontaneous reactivation of location-specific assemblies in entorhinal and hippocampal regions (Fig. 2a). These reactivations replayed the encoded sequence (A–D) in compressed form, shortening from 1.125 s (Fig. 1c) to less than 400 ms (Fig. 2b–g), as observed empirically [97]. Replay initiated mainly during SWS up-phases, concordant with empirical studies [98]. Sequential replay propagated downstream [99–101], mirroring delayed hippocampal activation during encoding (Fig. 1c). Partial replays (length < 4) outnumbered full replays (length $= 4$) (Fig. 2h), recapitulating empirical patterns [102]. CA3 generated replay sequences independently of MEC inputs [101]; MEC silencing (via 60-fold feedforward inhibition increase) reduced replay occurrences but preserved lengths and durations, echoing empirical findings [101]. Intra-regional inter-assembly delays exceed intra-assembly delays (Methods); eliminating them (set to 0 ms) disrupted sequential replays (Fig. 2i), underscoring their role in sequence maintenance [103].

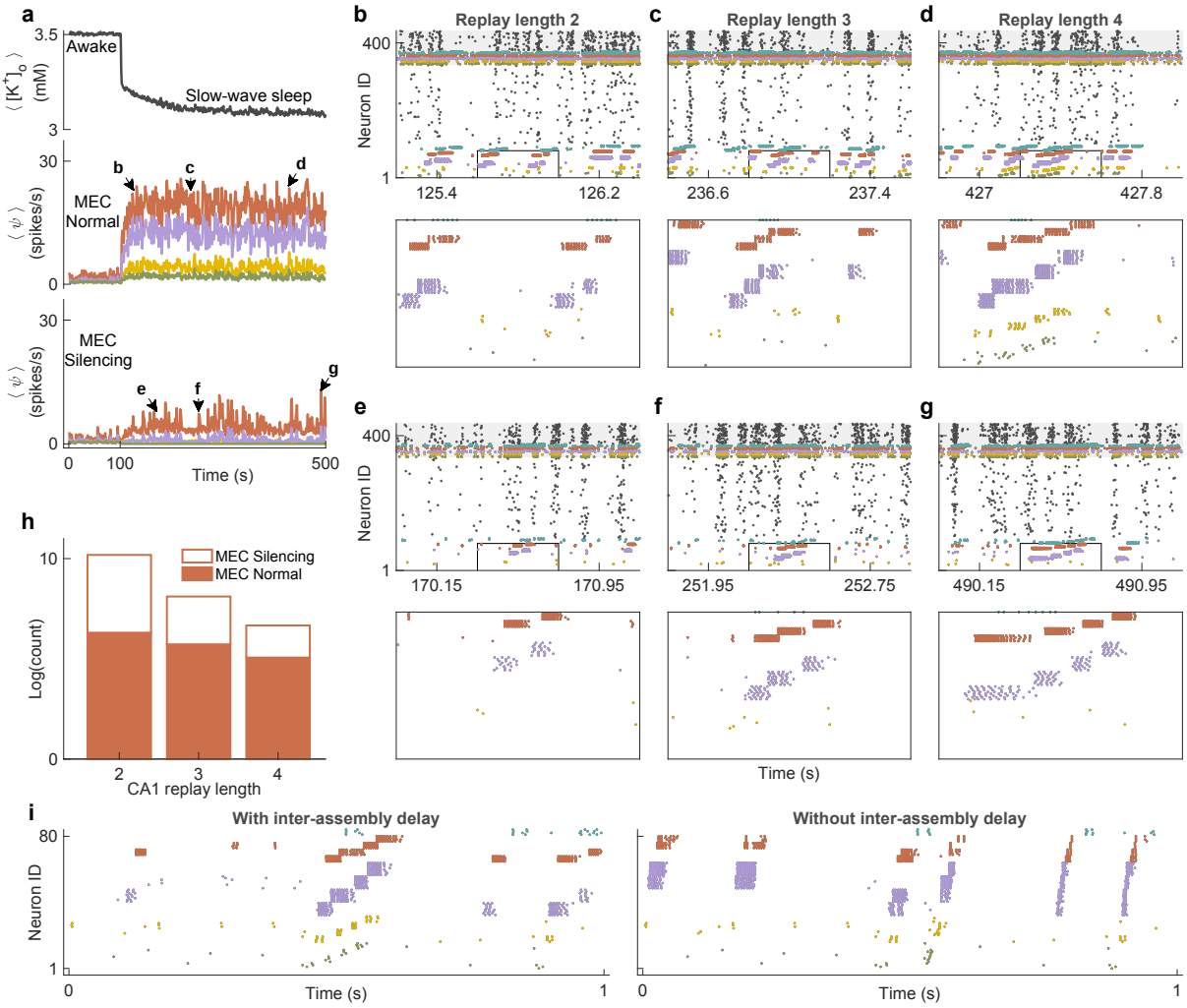

Fig 2: Transition to slow-wave sleep activates K^+-dependent disinhibition that enables spontaneous time-compressed replay via inter-assembly delay. a Time courses of average extracellular K^+, $\langle [K^+]_o \rangle$, and average firing rate of entorhinal and hippocampal regions. Top: Temporal evolution of $\langle [K^+]_o \rangle$ from 'Background' neurons when $[K^+]_{Buffer}$ is decreased from 3.5 to 3.0 mM at 100 s to initiate the transition from 'awake' to 'slow-wave sleep' dynamics. Middle & bottom: Average firing rates, $\langle \psi \rangle$, during normal MEC dynamics (middle) and during silenced MEC dynamics by enhanced inhibition (bottom). Arrows labeled 'b' to 'g' point to the timestamps of rasters in panels **b** to **g**. **b–g** Top: 1200 ms raster plot of spikes from all neurons at the respective timestamps from panel **a**. Bottom: Zoom of the 400 ms box from the top panel showing exemplars of replays with lengths 2–4. **h** Bar plot showing the logarithm of total number of CA1 replays of lengths 2–4 during time-courses in panel **a**. **i** Left: Sequential replay with inter-assembly delay. Right: Disrupted replay sequence without inter-assembly delay. Colors represent brain regions as in Fig. 1.

Reduced CA1 excitatory input yields ripple-less replay and decelerates synaptic consolidation, until disruption

Synchronized assembly bursts during replay evoke sharp-wave ripple (SWR)-like oscillations in simulated LFPs, originating in CA3 [44, 104–107] and propagating to CA1 [41, 104, 108, 109], as shown by frequency-time analyses (Fig. 3a). Motivated by ripple-less replays in non-salient contexts [45], we attenuated CA3→CA1 excitatory input without modeling saliency sources. This abolished ripples while preserving replay sequences (Fig. 3b), consistent with diminished ripples in salience-impaired states [110–114].

Although both ripple-associated and ripple-less replays consolidate hippocampal engram synapses by enhancing w via triplet-STDP and $\widetilde{w}$ via PRP consumption (Fig. 3a,b;

Methods), ripple-less replays at intermediate CA3→CA1 weight reduction (0.17×) consolidate slowly (functional), as triplet-STDP induces weaker potentiation at lower spike rates [77] and activity-dependent PRP synthesis (Methods) yields fewer PRPs for consumption (Fig. 3b). At higher reductions (0.13×), ripple-less replays persist but disrupt consolidation (dysfunctional; Fig. 3c).

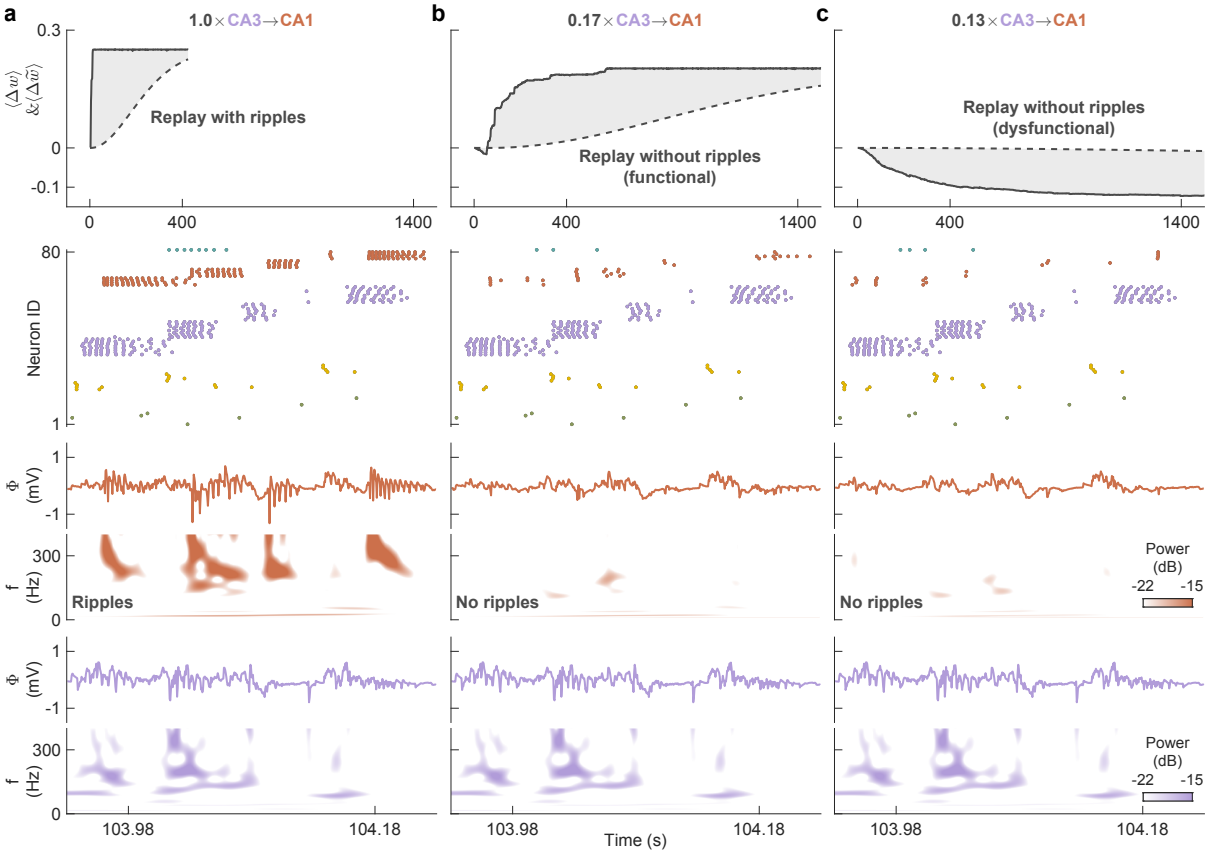

Fig 3: Reduced CA1 excitatory input renders replay without ripples, slowing synaptic consolidation, until disruption. **a–c** Dynamics with CA3→CA1 connectivity at 1.0× (a; with ripples), 0.17× (b; without ripples, functional), and 0.13× (c; without ripples, dysfunctional). Row 1: Time course of changes (Δ) in mean CA3→CA1 excitatory synaptic weights during slow-wave sleep ($\langle \Delta w \rangle$, solid, overall; $\langle \Delta \widetilde{w} \rangle$, dashed, stable; shading, labile; see Fig. 1d for details). Rows 2–6: 300-ms raster plot (row 2), local field potential and time-frequency analysis for CA1 (rows 3–4) and CA3 (rows 5–6) showing an exemplar replay. Colors represent brain regions as in Fig. 1.

Lateral inhibition unifies empirically observed ripple diversity

To examine lateral inhibition (LI) effects at fixed reduced levels on CA1 ripple-associated replays, we disabled triplet-STDP and dynamic inhibitory updates to prevent interference with fixed LI values, while silencing MEC to isolate the CA3→CA1 circuit. LI modulation controls inter-assembly gap durations during sequence replay [115], with reductions that elevate average ripple power (Methods; Fig. 4a) [79]. At 100% LI, discrete ripple chains emerge as separable high-frequency bursts in frequency-time spectra, with successive events encoding adjacent assemblies (Fig. 4b, left), consistent with observed chains [99, 116, 117]. At 50% LI, shortened gaps concatenate fragments into prolonged ripples (Fig. 4b, middle), mirroring long-duration ripples [79, 105, 117]. At 0% LI, total fusion disrupts winner-takes-all dynamics [118–121], co-activating assemblies into disordered bursts (Fig. 4b, right), resembling ripples in schizophrenia models [122].

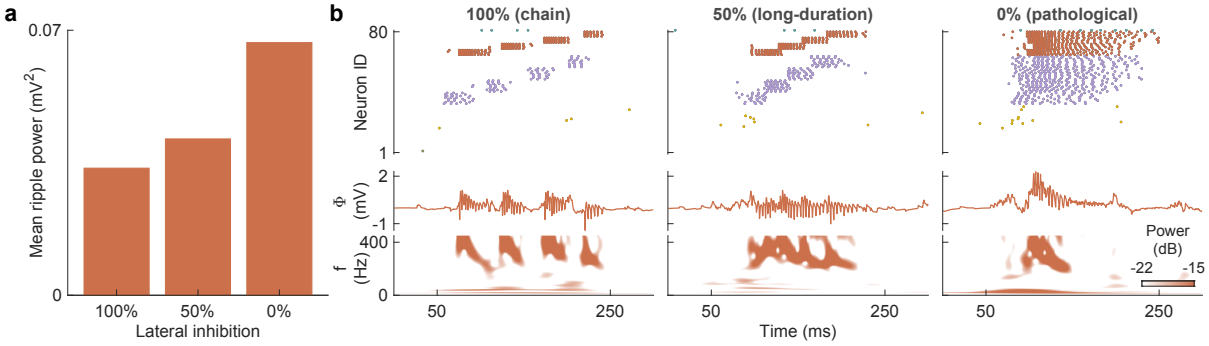

Fig 4: Different levels of lateral inhibition unify ripple diversity. **a** Mean power of CA1 ripple-associated replays (all lengths, including 1) increases as lateral inhibition (LI) decreases, computed over 200-s simulations. **b** 300-ms raster plot (row 1), CA1 local field potential (row 2), and CA1 frequency-time analysis (row 3) at 100% LI (ripple chain; left), 50% LI (long-duration ripple; middle), and 0% LI (pathological ripple; right). MEC is silenced to eliminate its inputs to CA3 and CA1, thereby isolating CA3 modulation of CA1. Colors represent brain regions as in Fig. 1.

Cortical disinhibition enables sequence transfer from hippocampus resulting in hippocampal independence

Systems consolidation involves the transfer of hippocampal memories to cortical regions (CRs) [38, 123–126], rendering them independent of the hippocampus [11, 37, 127, 128] for endurance despite hippocampal forgetting [13, 37, 129–131]. Sleep-modulated CR disinhibition enables CA1 ripple-associated replay to overcome strong feedforward inhibition active during wakefulness, which sequentially activates CR cell assemblies, thereby potentiating synapses to encode the transferred sequence (Fig. 5a) [54, 56, 132]. CR displays spontaneous replays even after silencing entorhinal and hippocampal regions, exhibiting hippocampal independence and confirming successful transfer.

Functional CA1 ripple-less replay transfers successfully to CR but more slowly than ripple-associated replay (Fig. 5b). However, dysfunctional ripple-less replay fails to achieve systems consolidation (Fig. 5c), but doubling CA1→CR excitatory weights restores consolidation (Fig. 5d), with implications for salience-impaired conditions where disrupted ripples hinder this process [110–114, 133].

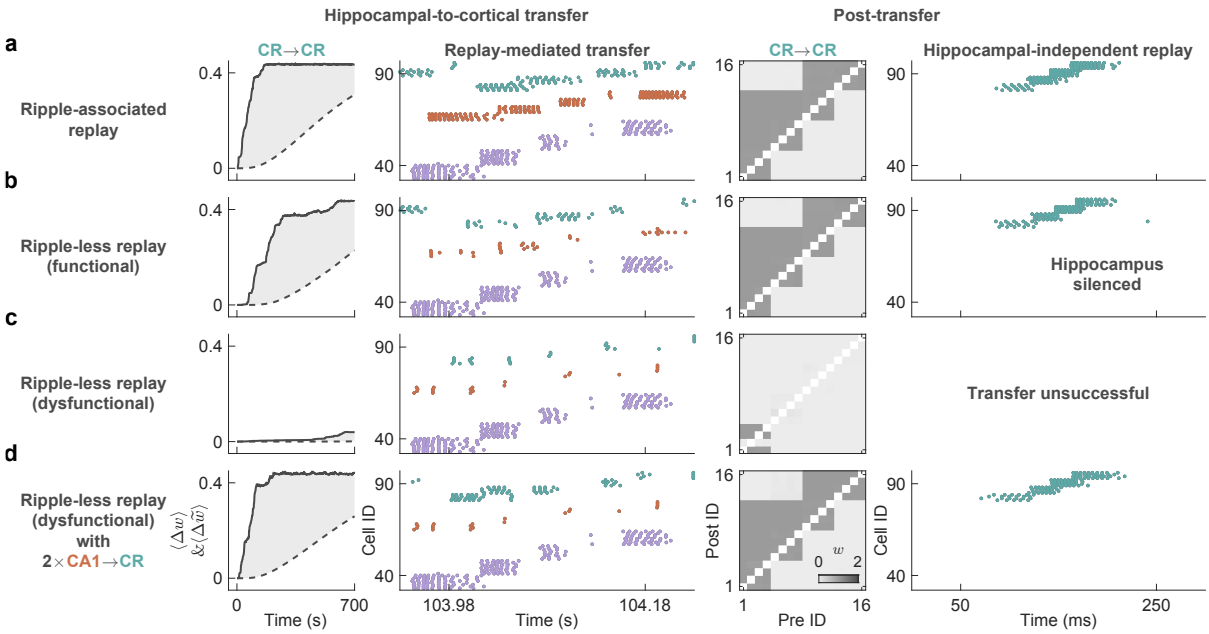

Fig 5: Hippocampal-to-cortical transfer via ripple-associated and ripple-less replay enables hippocampal independence. **a–d** Dynamics under ripple-associated replay (panel **a**), functional ripple-less replay (panel **b**), dysfunctional ripple-less replay (panel **c**), and dysfunctional ripple-less replay with doubled CA1→CR excitatory strength (panel **d**). Columns 1–2 trace the transfer: time course of changes (Δ) in mean CR→CR excitatory weights (column 1); 300-ms raster plot from Fig. 1 including CR neurons, depicting replay-mediated memory transfer to cortical assemblies (column 2). Columns 3–4 reveal post-transfer cortical autonomy: CR→CR excitatory weight matrix encoding transferred engram (column 3); hippocampal-independent replay after silencing MEC, DG, CA3, and CA1 through 60-fold feedforward inhibition increase, underscoring self-sustained CR replay (column 4). Colors denote brain regions as in Fig. 1.

Absent CA1 disinhibition explains MEC-input-dependent quiet wakefulness replay via MEC-mediated disinhibition

To explain why extended quiet wakefulness (QW) replay in hippocampal CA1 requires direct MEC inputs [99], we ablated MEC→CA1 excitatory and inhibitory connections. Despite this, CA3-initiated replay propagated to CA1, recapitulating MEC-independent sleep replay [99] (Fig. 6a).

In QW, neuromodulation-associated disinhibition is lower relative to sleep [56, 134, 135]. Disabling CA1 disinhibition eliminates replay propagation, irrespective of MEC and CA3 inputs (Fig. 6a). This conflicts with empirical observations where combined MEC and CA3 inputs enable QW replay, prompting the inclusion of MEC-mediated disinhibition to compensate for the absent sleep-modulated disinhibition. We connected MEC-recipient CA1 interneuron to inhibit CA3-recipient interneuron, inducing transient feedforward disinhibition (Fig. 6b) [136–138]. This restores CA3-elicited CA1 replay under disabled CA1 disinhibition but with concurrent MEC inputs, thus replicating MEC-input dependence in QW replay dynamics (Fig. 6b). Restoring sleep-modulated CA1 disinhibition eliminates MEC-input requirement while retaining CA3 dependence, matching empirical sleep replay [99].

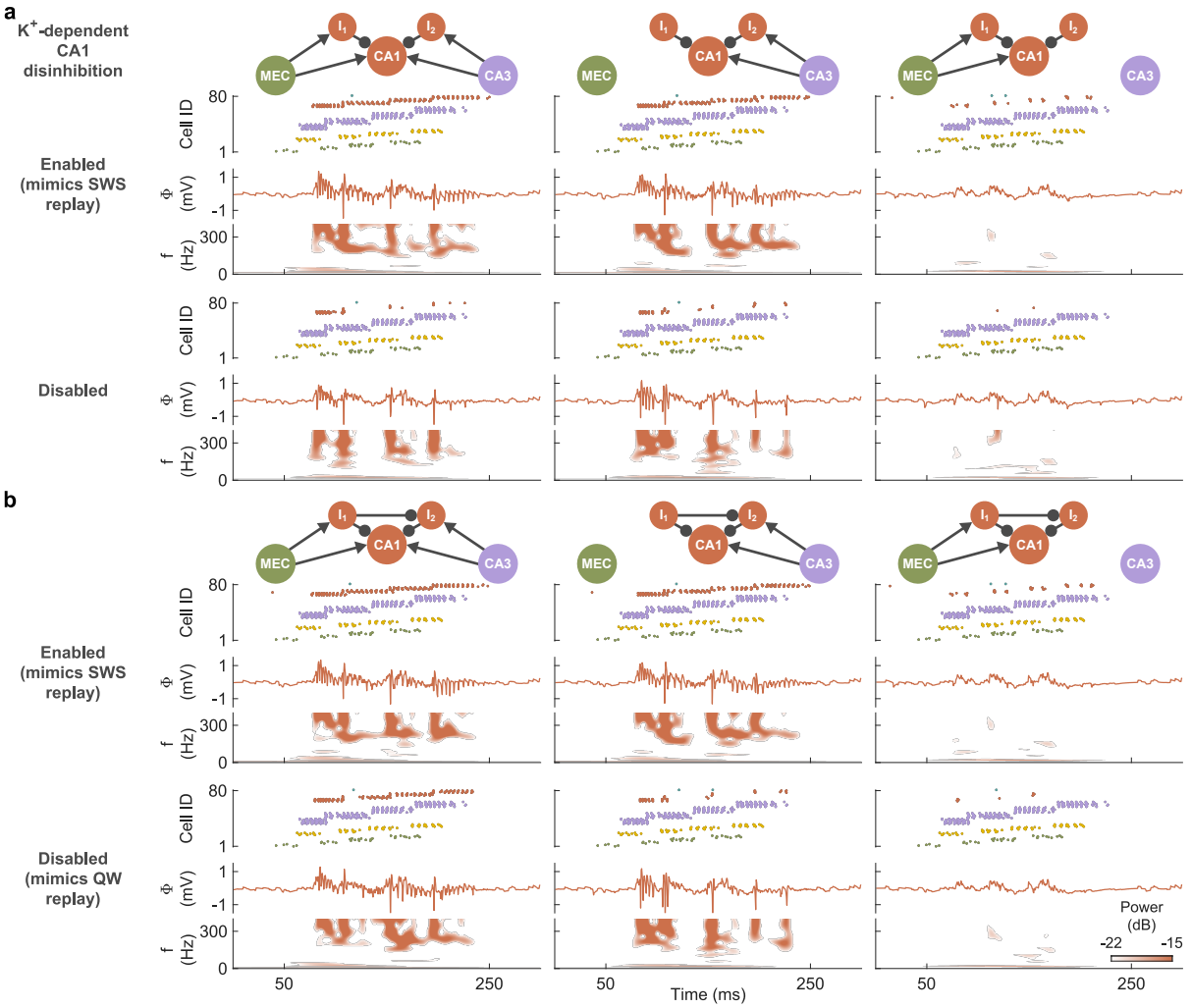

Fig 6: Disabling K^+-dependent CA1 disinhibition underlies MEC-input-dependent quiet wakefulness replay through MEC-mediated disinhibition. a,b Row 1: Schematics of feedforward excitatory inputs (arrows) from MEC and CA3 (column 1), CA3-only (column 2), or MEC-only (column 3) to CA1 excitatory and inhibitory neurons; absent (panel **a**) or present (panel **b**) inhibitory link (round arrowheads) from MEC- to CA3-receiving CA1 interneurons ($I_1 \rightarrow I_2 = 50$), enabling MEC-mediated disinhibition of excitatory CA1 neurons and gating CA3 input to CA1. Rows 2–7: Replay dynamics, with K^+-dependent disinhibition enabled (rows 2–4) or disabled (rows 5–7), in 300-ms raster plots (rows 2, 5), CA1 local field potentials (rows 3, 6), and time–frequency analyses (rows 4, 7). Colors denote brain regions as in Fig. 1.

Artificially induced disinhibition during wakefulness triggers memory processes driving consolidation

Memory replay, SWRs, and hippocampal-to-cortical transfer, typically sleep-associated, also occur during QW [123, 139–142]. To assess if disinhibition suffices to drive these memory processes independent of sleep-specific dynamics, we artificially induced disinhibition in entorhinal, hippocampal, and cortical regions under the derived QW replay parameters—disabled CA1 disinhibition and enabled MEC-mediated CA1 disinhibition—while preserving wakeful asynchronous background activity. This triggers spontaneous replays that achieve synaptic consolidation and hippocampal-to-cortical transfer for systems consolidation (Fig. 7), recapitulating sleep-associated processes. Thus, sustained disinhibition, not SWS up-down states [98], is fundamental across brain states for eliciting replay, ripples, and hippocampal-to-cortical transfer [54, 56, 132].

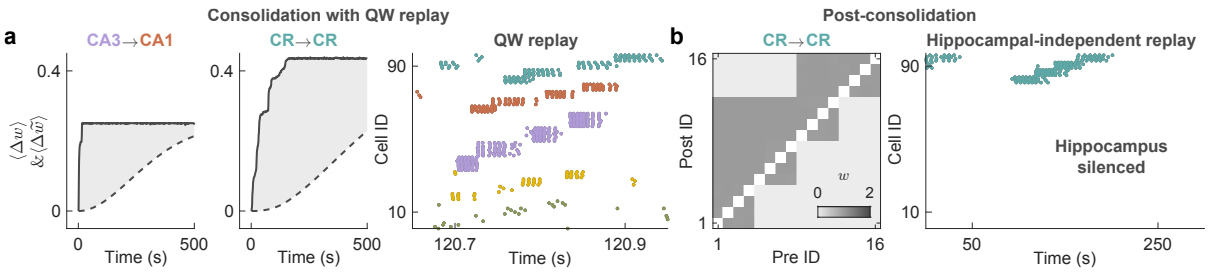

Fig 7: Artificially induced disinhibition under derived QW replay parameters drives synaptic and systems consolidation, yielding hippocampal independence. **a** QW replay-mediated consolidation: time course of changes (Δ) in mean synaptic weights of CA3→CA1 (left) and CR→CR (middle); raster plot of entorhinal, hippocampal, and cortical replays (right). **b** Post-consolidation cortical autonomy: CR→CR synaptic weight matrix encoding transferred engram (left); hippocampal-independent CR replay upon silencing MEC, DG, CA3, and CA1 (right). Colors denote brain regions as in Fig. 1.

Discussion

Our computational model reveals how sleep-modulated disinhibition coordinates memory consolidation through spontaneous replay events that promote synaptic strengthening and systems-level transfer. We mimic slow-wave sleep (SWS) by reducing extracellular potassium concentration ($[K^+]_o$), which lowers neuronal excitability [85] via a shift from high- to low-conductance states [143, 144]. This reduction diminishes neuromodulatory tone [145], thereby weakening inhibition [49, 55] and initiating up-down states [89]. Instead of disfacilitation [146] or inhibitory buildup [147] to terminate up states, with resurgence via recovery from disfacilitation [148] or rebound bursts [149], our model generates up states via disinhibition and terminates them through short-term depression [150] under baseline low-$[K^+]_o$ conditions. This posits that up-down states emerge from homeostatic compensation for sleep's low excitability and firing-rate reductions via disinhibition [151]—an activity-dependent neuromodulatory process that may presage persistent maladaptive disinhibition in disorders such as Alzheimer's disease [152], epilepsy [153], and others [154–156], wherein chronic low activity triggers inhibitory weakening via synaptic remodeling. This homeostatic view, echoed in computational studies [157–160], proposes in vivo experiments inducing low excitability—via pharmacological Na^+ channel blockade [161], genetic overexpression of Kir4.1 in astrocytes [162], or optogenetic neuronal hyperpolarization [163]—to verify if this elicits disinhibition [164] and up-down states independently of natural sleep. In Alzheimer's disease, astrocyte dysfunction disrupts K^+ buffering [165], correlating with SWS fragmentation that accelerates pathological progression [166]; our K^+ buffering model, supported by optogenetic astrocyte interventions restoring sleep rhythms [167], suggests that boosting astrocytic Kir4.1 function may stabilize SWS cycles and ameliorate memory deficits, given that its impairment aggravates disease features [168].

Complementing prior models of slow synaptic weight stabilization [158, 160], our offline consolidation integrates activity-dependent protein synthesis for slow-timescale engram stability [83] and spontaneous replays that engage fast-timescale triplet-STDP for selective engram strengthening [169]. The model's sustained disinhibition—distinct from transient variants in ripple initiation [41, 42, 170] and gating hippocampal-to-cortical input [47]—engages dedicated pathways for engram sequence replay, sharp-wave ripple (SWR) generation, and hippocampal-to-cortical transfer. In contrast to views positing

SWRs as replay initiators [43, 44], we identify independent mechanisms: inter-assembly delays drive sequential reactivation, while lateral inhibition preserves assembly separation, enabling robust replay despite ripple absence (ripple-less replays [45]) upon CA1 excitatory afferent attenuation. Synaptic and systems consolidation persist in ripple-less replay, albeit at reduced rates, motivating empirical assays of selective ripple ablation via CA1 afferent weakening—unlike prior methods co-disrupting replays and ripples [67–72]—to disentangle their roles. Paralleling ripple-less replays of non-salient trajectories [45], these mechanisms suggest tunable adjustment of CA1 afferent strength to normalize ripple dynamics in salience-impaired conditions: enhancing where ripples diminish, as in Alzheimer's disease [110,111], epilepsy (physiological SWRs) [112,113], and aging [110,114]; attenuating where they surge, as in schizophrenia [122, 133, 171]. Amid hippocampal seizure risks [172], alternatively strengthening CA1-to-cortical connectivity restores engram transfer even with dysfunctional ripple-less replay. Future extensions could incorporate saliency cues from locus coeruleus (novelty) [173], ventral tegmental area (reward) [174], basal amygdala (emotion) [175], or lateral entorhinal cortex (contextual cues stabilizing ensembles) [176–178] to prioritize encoding of internally imagined [179] or externally sensed [174] events that deviate from anticipated offline replay [180, 181].

LI's modulation of inter-assembly gap duration during simulated sequence replay underlies ripple diversity: strong LI yields discrete chains (doublets, triplets) that link sequence fragments [99, 116, 117]; intermediate LI concatenates them into prolonged events preserving replay sequence [79, 105, 117]; weak LI induces fusion and sequence erosion—mirroring order-ablated patterns from parvalbumin interneuron silencing [39] and pathological disinhibition in schizophrenia [122,182]—positioning LI as a prime therapeutic target for restoring trajectory fidelity.

Neuromodulatory changes similar to those in SWS occur during quiet wakefulness (QW), albeit to a lesser extent [134], reducing inhibitory tone [56,135]. This disinhibition potentially explains delayed replays of recent experiences [31] by overcoming learning-induced inhibition. Our model reveals that MEC-mediated disinhibition compensates the disabled CA1 disinhibition to gate CA3 input and trigger ripple-associated replay, mirroring empirical MEC-input dependence during QW [31, 99]; whereas enabling CA1 disinhibition eliminates this MEC-input dependence, as seen in SWS replay [99]. This suggests reduced neuromodulator-driven CA1 disinhibition during QW relative to SWS, testable by optogenetically enhancing CA1 disinhibition to determine if MEC-input dependence is eliminated, akin to sleep dynamics [99]. Future models could incorporate CA1 recurrent connections [183] to explain MEC- and CA3-independent CA1 assembly sequences during active exploration [184], potentially triggered by contextual cues from lateral entorhinal cortex [176] and thalamic nucleus reuniens [185]. While SWS up-states create excitatory windows facilitating hippocampal ripples [186], our model demonstrates that artificially induced sustained disinhibition during wakefulness—independent of up-states—suffices to initiate and propagate ripple-associated replay to cortical regions [47,141]. This implies nuanced roles for cortical SWS up-states and associated sleep spindles, such as integrating transferred information across broader cortical networks [46], wherein spindle absence—by disrupting hippocampal input gating and inter-cortical integration—may drive consolidation deficits under sleep deprivation [187], a mechanism ripe for future modeling.

Although our model captures key hippocampal replay dynamics through recurrent MEC

and CA3 connections that encode sequential engram and initiate offline replay [60,188,189], it omits feedback projections, including cortical input for replay selection [38,190] and CA3→DG connectivity for dentate sharp wave [191]. Instead, feedforward input from MEC replay [188] yields underexplored DG patterns that recapitulate encoding-like sequential activation [192,193]. Extending MEC theta-phase precession could model reverse replay, with past assembly following current one to form backward association [194], abstractly resembling symmetrical STDP [60] despite asymmetric rules. The model couples inhibitory plasticity updates to excitatory-to-excitatory plasticity for excitation-inhibition balance, yet biologically observed independent local inhibitory rules [195] may intrinsically maintain this balance in future versions. During encoding, CA1 activity evokes transient cortical activation incapable of long-term potentiation [95,196], modeled via heightened feedforward inhibition, preventing premature cortical engram maturation [37]; refining short-term synaptic plasticity to strengthen cortical synapses on working memory timescales [197,198] could elucidate working memory's role in systems consolidation [199]. Broader extensions could explore preplay for engram recruitment [200] probably shaped by past experience [201], rapid eye movement engram dynamics for complementary consolidation [49], larger networks for multi-memory storage [87,158], and gradual forgetting [13,37,202] via neurogenesis-driven processes [129,203–205] that facilitate systems reconsolidation to update memories [204], increasing selectivity [160], and promoting generalization with low-dimensional concept retention [12,15,206–208].

Methods

Individual neuronal dynamics

The core dynamics of each neuron revolve around its membrane potential V (in mV), the electrical voltage across the cell's membrane that governs action potential initiation, described by the stochastic Hodgkin-Huxley equation [76,209]:

$$C\,dV = I\,dt + I_{\text{noise}}, \tag{1}$$

where C (in μF/cm^2) is the membrane capacitance, dV is the infinitesimal change in V, dt is the infinitesimal time interval, $I = -I_{\text{Na}} - I_{\text{K}} - I_{\text{Cl}} - I_{\text{syn}}$ is the deterministic current (in μA/cm^2) comprising the sodium current I_{Na} (usually inward, initiating depolarization), the potassium current I_{K} (usually outward, enabling repolarization), the chloride leak current I_{Cl} (usually outward at rest, stabilizing baseline V), and the synaptic current I_{syn} (inward for excitatory or outward for inhibitory signals), and $I_{\text{noise}} = \sigma_{\text{noise}} C\,dW$ is the stochastic current with dW (in $\sqrt{\text{ms}}$) normally distributed with mean zero and variance dt, and σ_{noise} (in mV/$\sqrt{\text{ms}}$) scaling the noise amplitude. This stochastic term approximates net current perturbations from thermal fluctuations driving random ion channel gating [210] and synaptic neurotransmitter release [211]. The equation captures how depolarizing/hyperpolarizing current balance, augmented by noise, drives V dynamics and action potential firing when depolarization prevails.

The ionic currents flow through specialized protein channels in the membrane, modeled

as

$$I_{\mathrm{Na}} = G_{\mathrm{Na}} m^3 h (V - E_{\mathrm{Na}}) + G_{\mathrm{NaL}} (V - E_{\mathrm{Na}}), \tag{2}$$
$$I_{\mathrm{K}} = G_{\mathrm{K}} n^4 (V - E_{\mathrm{K}}) + G_{\mathrm{KL}} (V - E_{\mathrm{K}}), \tag{3}$$
$$I_{\mathrm{Cl}} = G_{\mathrm{ClL}} (V - E_{\mathrm{Cl}}), \tag{4}$$

where G_{Na} (in mS/cm^2) and G_{K} (in mS/cm^2) are the maximum possible flow rates (conductances) through sodium and potassium channels when they are fully open during an action potential. G_{NaL} (in mS/cm^2), G_{KL} (in mS/cm^2), and G_{ClL} (in mS/cm^2) are small, constant leak conductances that allow baseline ion flow, contributing to the neuron's resting membrane potential. The variables m, h, and n are fractions between 0 and 1 that represent the proportion of channels in an open or active state: m increases to open sodium channels as V becomes less negative (depolarizes), h decreases to inactivate sodium channels and limit the duration of the action potential, and n increases with a delay to open potassium channels and return V to rest. The exponents (such as m^3h) reflect that multiple molecular subunits must align for a channel to open fully. E_{Na}, E_{K}, and E_{Cl} are the reversal potentials for each ion, the specific voltage values at which the net flow of that ion stops because electrical and concentration forces balance (typically positive for E_{Na} favoring inward flow, and negative for E_{K} and E_{Cl} favoring outward flow).

The fractions m, h, and n adjust dynamically over time based on V:

$$\frac{dm}{dt} = \alpha_m (1 - m) - \beta_m m, \tag{5}$$
$$\frac{dh}{dt} = \alpha_h (1 - h) - \beta_h h, \tag{6}$$
$$\frac{dn}{dt} = \alpha_n (1 - n) - \beta_n n, \tag{7}$$

where these equations describe how the fractions approach steady states: the α terms increase the fraction toward 1 (opening or activating the channel), while the β terms decrease it toward 0 (closing or inactivating the channel). This allows channels to open quickly during depolarization and close during repolarization. The rates α and β vary with the membrane potential V [212, 213]:

$$\alpha_m = \phi_{\alpha m} \frac{V + V_{\mathrm{shift},\alpha m}}{1 - \exp\left\{-\frac{V + V_{\mathrm{shift},\alpha m}}{\sigma_{\alpha m}}\right\}}, \quad \beta_m = \phi_{\beta m} \frac{V + V_{\mathrm{shift},\beta m}}{\exp\left\{\frac{V + V_{\mathrm{shift},\beta m}}{\sigma_{\beta m}}\right\} - 1}, \tag{8}$$
$$\alpha_n = \phi_{\alpha n} \frac{V + V_{\mathrm{shift},\alpha n}}{1 - \exp\left\{-\frac{V + V_{\mathrm{shift},\alpha n}}{\sigma_{\alpha n}}\right\}}, \quad \beta_n = \phi_{\beta n} \exp\left\{-\frac{V + V_{\mathrm{shift},\beta n}}{\sigma_{\beta n}}\right\}, \tag{9}$$
$$\alpha_h = \phi_{\alpha h} \exp\left\{-\frac{V + V_{\mathrm{shift},\alpha h}}{\sigma_{\alpha h}}\right\}, \quad \beta_h = \frac{\phi_{\beta h}}{1 + \exp\left\{-\frac{V + V_{\mathrm{shift},\beta h}}{\sigma_{\beta h}}\right\}}, \tag{10}$$

where the ϕ parameters (in ms^{-1}) set the baseline magnitude of each rate, V_{shift} adjusts the voltage level at which the rate reaches half its maximum to align with typical neuronal firing thresholds (e.g., -50 mV), and σ determines how sensitively the rate responds to small changes in V (smaller values mean sharper responses).

The reversal potentials depend on ion concentrations across the membrane, following the Nernst equation:

$$E_{\mathrm{Na}} = \frac{RT}{F} \ln \left(\frac{[\mathrm{Na}^+]_{\mathrm{o}}}{[\mathrm{Na}^+]_{\mathrm{i}}} \right), \tag{11}$$

$$E_{\mathrm{K}} = \frac{RT}{F} \ln \left(\frac{[\mathrm{K}^+]_{\mathrm{o}}}{[\mathrm{K}^+]_{\mathrm{i}}} \right), \tag{12}$$

$$E_{\mathrm{Cl}} = \frac{RT}{F} \ln \left(\frac{[\mathrm{Cl}^-]_{i}}{[\mathrm{Cl}^-]_{o}} \right), \tag{13}$$

where R (in J/mol·K) is the universal gas constant, T (in K) is the absolute temperature, and F (in C/mol) is Faraday's constant. Chloride concentrations are held constant for simplicity, while sodium and potassium levels vary with neuronal activity, as described below.

Ion concentrations evolve as ions move through channels during action potentials and are restored by pumps [212]:

$$\frac{d[\mathrm{K}^+]_{\mathrm{o}}}{dt} = \gamma\beta I_{\mathrm{K}} - 2\beta I_{\mathrm{pump}} - \epsilon_{\mathrm{K}} \left([\mathrm{K}^+]_{\mathrm{o}} - [\mathrm{K}^+]_{\mathrm{Buffer}} \right), \tag{14}$$

$$\frac{d[\mathrm{Na}^+]_{\mathrm{i}}}{dt} = -\gamma I_{\mathrm{Na}} - 3I_{\mathrm{pump}}, \tag{15}$$

$$\frac{d[\mathrm{Na}^+]_{\mathrm{o}}}{dt} = \gamma\beta I_{\mathrm{Na}} + 3\beta I_{\mathrm{pump}} - \epsilon_{\mathrm{Na}} \left([\mathrm{Na}^+]_{\mathrm{o}} - [\mathrm{Na}^+]_{\mathrm{Buffer}} \right), \tag{16}$$

where γ is a conversion factor that translates electrical current measurements (in μA/cm^2) into changes in ion concentration (in mM/s), based on cell size and charge per ion; β is the ratio of the cell's internal volume to the surrounding external space, reflecting that the external space is smaller and thus more prone to rapid concentration shifts; and I_{pump} is the current generated by the sodium-potassium pump, a protein that actively moves 3 sodium ions out and 2 potassium ions in per cycle to counteract imbalances from firing. The terms with ϵ_{K} (in s^{-1}) (potassium clearance rate) and ϵ_{Na} (in s^{-1}) (sodium clearance rate) model diffusion and buffering that pull external potassium and sodium toward $[\mathrm{K}^+]_{\mathrm{Buffer}}$ and $[\mathrm{Na}^+]_{\mathrm{Buffer}}$, respectively—stable reference concentrations representing the combined stabilizing effects of nearby blood vessels, tissues, and support cells like astrocytes.

Assuming total ion conservation [212, 213], achieved by balancing inward Na^+ flux with outward K^+ flux, the intracellular K^+ concentration, $[\mathrm{K}^+]_{\mathrm{i}}$, is given by:

$$[\mathrm{K}^+]_{\mathrm{i}} = \mathrm{K}_{\mathrm{i,base}} + (\mathrm{Na}_{\mathrm{i,ref}} - [\mathrm{Na}^+]_{\mathrm{i}}), \tag{17}$$

where $\mathrm{K}_{\mathrm{i,base}}$ is the resting intracellular K^+ level and $\mathrm{Na}_{\mathrm{i,ref}}$ is a reference intracellular Na^+ level.

The pump current, I_{pump}, increases gradually (in a sigmoidal pattern) as $[\mathrm{Na}^+]_{\mathrm{i}}$or $[\mathrm{K}^+]_{\mathrm{o}}$levels rise, mimicking how the pump ramps up to restore balance:

$$I_{\mathrm{pump}} = \frac{\rho_{\mathrm{max}}}{\left(1 + \exp\left\{\frac{\mathrm{Na}_{\mathrm{th}} - [\mathrm{Na}^+]_{\mathrm{i}}}{\sigma_{\mathrm{Na}}}\right\}\right)\left(1 + \exp\left\{\mathrm{K}_{\mathrm{th}} - [\mathrm{K}^+]_{\mathrm{o}}\right\}\right)}, \tag{18}$$

where $\rho_{\max}$ (in mM/s) is the pump's maximum operating speed, $\mathrm{Na_{th}}$ and $\mathrm{K_{th}}$ are the concentration levels at which the pump reaches half-speed, and σ_{Na} controls how abruptly the pump responds to sodium increases.

The synaptic current, I_{syn}, aggregates inputs from P^{ex} presynaptic excitatory neurons [214–217]:

$$I_{\mathrm{syn}} = \sum_{j=1}^{P^{\mathrm{ex}}} G_{j\to\mathrm{post}}\,(V - E_j)\,\mathrm{S}j e^{-\frac{\chi j}{\tau_{\mathrm{att}}}}, \tag{19}$$

where $G_{j\to\mathrm{post}}$ is the maximum synaptic conductance for synapses between postsynaptic (excitatory or inhibitory) and the jth presynaptic (excitatory or inhibitory) neurons, E_j is the reversal potential (typically positive for excitatory, producing inward depolarizing currents at resting potential; negative for inhibitory, producing outward hyperpolarizing currents at resting potential), S_j is the fraction (ranging from 0 to 1) of open postsynaptic channels at the synapses formed with the jth presynaptic neuron, and the exponential term attenuates synaptic strength when the presynaptic neuron is in depolarization block, with χ_j integrating a voltage-dependent measure of the duration of the depolarization block and τ_{att} setting the attenuation scale. S_j depends on the presynaptic neuron's voltage, V_j, following first-order kinetics [213–215]:

$$\tau_{\mathrm{ex/inh}}\frac{d\mathrm{S}_j}{dt} = \frac{T_{\max}}{1+\exp\left\{-\frac{V_j+V_{\mathrm{shift,S}}}{\sigma_{\mathrm{S}}}\right\}}(1-\mathrm{S}_j) - \mathrm{S}_j, \tag{20}$$

where $\tau_{\mathrm{ex/inh}}$ is the decay time scale for excitatory/inhibitory synapses, $T_{\max}$ is the maximum neurotransmitter release rate, $V_{\mathrm{shift,S}}$ adjusts the presynaptic voltage for half-maximal release, and σ_{S} sets how sharply release responds to V_j changes. The dynamics of χ_j are governed by:

$$\frac{d\chi_j}{dt} = \eta_\chi(V_j + V_{\mathrm{shift},\chi}) - \delta_\chi \chi_j, \tag{21}$$

where η_χ equals $\eta_{\max}$ if the presynaptic membrane potential V_j falls within the depolarization block range ($V_{\mathrm{dep,low}}$ to $V_{\mathrm{dep,high}}$) and 0 otherwise, $V_{\mathrm{shift},\chi}$ is a voltage shift that modulates the buildup rate, and δ_χ is the decay rate of χ_j that restores synaptic strength post-block and prevents overload during prolonged block.

Maximal synaptic conductances, $G_{\mathrm{pre}\to\mathrm{post}}$, depend on short-term and long-term plasticity states:

$$G_{\mathrm{ex}\to\mathrm{post}} = g_{\mathrm{ex}\to\mathrm{post}}\; w_{\mathrm{ex}\to\mathrm{post}}\; x_{\mathrm{ex}}\; u_{\mathrm{ex}}\; y_{\mathrm{post}}, \tag{22}$$

$$G_{\mathrm{inh}\to\mathrm{post}} = g_{\mathrm{inh}\to\mathrm{post}}\; w^{\mathrm{mod}}_{\mathrm{inh}\to\mathrm{post}}, \tag{23}$$

where $g_{\mathrm{pre}\to\mathrm{post}}$ is the maximal synaptic conductance per single spine for connections between postsynaptic ('post') and presynaptic ('pre') neurons; x, u, and y are short-term plasticity states; $w_{\mathrm{ex}\to\mathrm{post}}$ is the excitatory synaptic weight; and $w^{\mathrm{mod}}_{\mathrm{inh}\to\mathrm{post}}$ is the state-dependent modulation of the inhibitory weight.

Addition and removal of spines

Synaptic weights, $w_{\text{pre}\to\text{post}}$, represent postsynaptic receptor density across spines, including both protein synthesis-dependent stable (late long-term potentiation; late-LTP) and protein synthesis-independent labile (early long-term potentiation; early-LTP) components, with $\widetilde{w}_{\text{pre}\to\text{post}}$ denoting only the stable receptor density (late-LTP) [158]. For excitatory-to-excitatory connections, the variable, $L_{\text{pre}\to\text{post}}$, represents the number of spines (each holding up to one unit of receptor density when at peak), capping the maximum allowable potentiation in $w_{\text{pre}\to\text{post}}$.

During potentiation attempts in an excitatory-to-excitatory connection, if all spines reach peak receptor density (i.e., $w_{\text{pre}\to\text{post}}$ approaches $L_{\text{pre}\to\text{post}}$) but are not fully stabilized (i.e., $\widetilde{w}_{\text{pre}\to\text{post}} < L_{\text{pre}\to\text{post}}$), no potentiation occurs. However, if the receptor density is stabilized ($\widetilde{w}_{\text{pre}\to\text{post}}$ approaches $L_{\text{pre}\to\text{post}}$) through protein-dependent processes, a new spine is added by incrementing $L_{\text{pre}\to\text{post}}$ by 1, potentially by inducing spine remodeling, allowing further receptor density increases. This ensures receptor density is sequentially allocated across spines by saturating them to full capacity (1 unit each) before distributing any remainder to an additional spine.

Conversely, during depression, as $w_{\text{pre}\to\text{post}}$ decreases, the receptor density in one or more spines may reach zero. Upon stabilization of these changes (reflected in $\widetilde{w}_{\text{pre}\to\text{post}}$), the number of spines is adjusted according to

$$L_{\text{pre}\to\text{post}} = \min(L_{\text{pre}\to\text{post}}, \lceil \widetilde{w}_{\text{pre}\to\text{post}} \rceil + 1), \tag{24}$$

where the ceiling function, $\lceil \widetilde{w}_{\text{pre}\to\text{post}} \rceil$, determines the minimum number of spines required to accommodate the stable receptor density. Adding $+1$ permits at most one spine with zero stable receptor density, effectively deleting excesses in $L_{\text{pre}\to\text{post}}$ that would yield more than one such spine. The min operation prevents premature addition of new spines; for instance, if $L_{\text{pre}\to\text{post}} = 1$ and $\widetilde{w}_{\text{pre}\to\text{post}} = 0.1$, $L_{\text{pre}\to\text{post}}$ remains 1, avoiding interference with the addition mechanism. This mechanism facilitates the removal of redundant non-functioning spines while preserving the minimal viable synaptic structure and mirrors empirical observations in biological synapses where repetitive long-term depression leads to pruning of spines with stably reduced receptor density [84].

Excitatory-to-excitatory long-term plasticity

Synaptic weights, $w_{\text{pre}\to\text{post}}$, are updated using a triplet spike-timing-dependent plasticity rule [77] . Upon a presynaptic spike, weights to postsynaptic neurons are depressed proportionally to the product of the fast postsynaptic trace, $z_{\text{post}}^{\text{fast}}$, and a term combining pair-based and triplet-based depression factors:

$$\Delta w^{-}_{\text{pre}\to\text{post}} = -\eta_w \cdot z_{\text{post}}^{\text{fast}} \cdot (A_2^- + A_3^- \cdot z_{\text{pre}}^{\text{slow}}), \tag{25}$$

where A_2^- is the pair-based depression amplitude, and A_3^- is the triplet-based depression amplitude.

Conversely, upon a postsynaptic spike, weights from presynaptic neurons are potentiated similarly:

$$\Delta w^{+}_{\text{pre}\to\text{post}} = \eta_w \cdot z^{\text{fast}}_{\text{pre}} \cdot (A^{+}_{2} + A^{+}_{3} \cdot z^{\text{slow}}_{\text{post}}), \tag{26}$$

where A^{+}_{2} is the pair-based potentiation amplitude, and A^{+}_{3} is the triplet-based potentiation amplitude.

Synaptic traces are modeled as low-pass filters of spike trains [158], evolving according to:

$$\frac{d}{dt} z^{\tau} = -\frac{z^{\tau}}{\tau_z} + \sum \delta(t - t^{\text{spike}}), \tag{27}$$

where z^{τ} is the trace with time constant τ_z (in ms) ($\tau^{\text{fast}}_{\text{pre}}$ and $\tau^{\text{fast}}_{\text{post}}$ for fast traces capturing recent activity, $\tau^{\text{slow}}_{\text{pre}}$ and $\tau^{\text{slow}}_{\text{post}}$ for slow traces capturing earlier activity). In the update rules, the fast presynaptic trace, $z^{\text{fast}}_{\text{pre}}$, is evaluated at the current spike time t, while the other three traces ($z^{\text{fast}}_{\text{post}}$, $z^{\text{slow}}_{\text{pre}}$, $z^{\text{slow}}_{\text{post}}$) are evaluated just prior to t to exclude the current spike. This offset ensures that depression reflects only presynaptic spikes preceded by postsynaptic activity, potentiation dominates without cancellation when spikes coincide, and slow traces incorporate solely prior spikes.

The learning rate, η_w, is scaled such that plasticity is enhanced only when both presynaptic and postsynaptic firing rates—f_{pre} and f_{post} (computed as synaptic traces with a time-constant of 1 s; z^1)—significantly exceed their baseline rates [218, 219], $f_{\text{ref,pre}}$ and $f_{\text{ref,post}}$, by a factor of c_η:

$$\eta_w = \frac{1}{1 + \exp\left(-s_\eta \left(\frac{f_{\text{post}}}{c_\eta \cdot f_{\text{ref,post}}} - k_\eta\right)\right)} \cdot \frac{1}{1 + \exp\left(-s_\eta \left(\frac{f_{\text{pre}}}{c_\eta \cdot f_{\text{ref,pre}}} - k_\eta\right)\right)}, \tag{28}$$

where s_η is the steepness parameter, and k_η is the midpoint threshold.

Inhibitory long-term plasticity mechanisms

Dynamic feedforward inhibition

To preserve excitation-inhibition balance, modifications to excitatory-to-excitatory synaptic weights are mirrored by coordinated adjustments in the feedforward inhibitory circuitry [78]. When the weight, $w_{\text{pre}\to\text{post}}$, changes by $\Delta w^{\pm}_{\text{pre}\to\text{post}}$ (positive for potentiation, negative for depression), the excitatory-to-inhibitory weights, $w_{\text{pre}\to\text{I}_\text{j}}$, and inhibitory-to-excitatory weights, $w_{\text{I}_\text{j}\to\text{post}}$, involving the M inhibitory interneurons that form feedforward paths are updated according to:

$$\Delta w_{\text{pre}\to\text{I}_\text{j}} = \frac{a}{M} \cdot \Delta w^{\pm}_{\text{pre}\to\text{post}}, \tag{29}$$

$$\Delta w_{\text{I}_\text{j}\to\text{post}} = \frac{b}{M} \cdot \Delta w^{\pm}_{\text{pre}\to\text{post}}, \tag{30}$$

where $j = 1$ to M indexes the interneurons, and a and b are scaling constants. These coupled updates ensure proportional scaling of inhibitory drive in response to excitatory changes.

Dynamic feedback and lateral inhibition

In non-background regions (entorhinal, hippocampal, and cortical), we employ distinct inhibitory neurons to mediate feedback [220] and lateral inhibition [221]. Each cell assembly in these regions is assigned one assembly-specific inhibitory neuron (ASIN), which provides feedback inhibition to excitatory neurons within its assembly and lateral inhibition to excitatory neurons in other assemblies, promoting winner-takes-all dynamics [79, 222]. The weights from 'post' to its ASIN, $w_{\text{post}\to\text{ASIN}}$; from the ASIN to each neuron in its assembly, $w_{\text{ASIN}\to\text{self}}$, for feedback inhibition; and from the ASIN to each neuron in other assemblies, $w_{\text{ASIN}\to\text{other}}$, for lateral inhibition are updated according to:

$$\Delta w_{\text{post}\to\text{ASIN}} = c \cdot \Delta w^{\pm}_{\text{pre}\to\text{post}}, \tag{31}$$

$$\Delta w_{\text{ASIN}\to\text{self}} = \frac{d}{N} \cdot \Delta w^{\pm}_{\text{pre}\to\text{post}}, \tag{32}$$

$$\Delta w_{\text{ASIN}\to\text{other}} = \frac{f}{N} \cdot \Delta w^{\pm}_{\text{pre}\to\text{post}}, \tag{33}$$

where N is the number of neurons in the assembly to which 'post' belongs; c, d, and f are scaling constants.

K^+-dependent disinhibition modulating factor

During sleep, extracellular potassium concentration ($[K^+]_o$) decreases [85], contributing to reduced neuronal excitability through membrane hyperpolarization [223]. Concurrently, acetylcholine levels drop to minimal values during deep sleep [56], unblocking M-current in interneurons and reducing their responsiveness to synaptic inputs [49]. In parallel, norepinephrine levels, reduced during sleep [224], diminish GABAergic inhibition [55], whereas high norepinephrine during wakefulness enhances it via adrenergic receptors [225].

To model this sleep-modulated weakening of inhibitory synaptic transmission without structural plasticity, we introduce a multiplicative modulating factor, denoted as $f_I([K^+]_o)$, evolving as a sigmoid function to ensure a smooth transition based on $[K^+]_o$ levels:

$$f_I([K^+]_o) = l_f + \frac{1 - l_f}{1 + \exp(-s_f \cdot (\langle [K^+]_o \rangle - k_f))}, \tag{34}$$

where $\langle [K^+]_o \rangle$ is the average $[K^+]_o$ in the background region, l_f is the minimum scaling value reached during slow-wave sleep (varying by region: MEC, DG, CA3, CA1, CR, Background), s_f (in mM^{-1}) is the steepness parameter of the sigmoid, and k_f (in mM) is the midpoint potassium concentration where the factor is halfway between l_f and 1. This factor scales the baseline I→E and I→I synaptic weights:

$$w^{\text{mod}}_{\text{inh}\to\text{ex}} = w_{\text{inh}\to\text{ex}}\, f_I([K^+]_o), \tag{35}$$

$$w^{\text{mod}}_{\text{inh}\to\text{inh}} = w_{\text{inh}\to\text{inh}}\, f_I([K^+]_o). \tag{36}$$

Short-term plasticity

Short-term synaptic plasticity in excitatory synapses is modeled using the Tsodyks-Markram framework for the presynaptic dynamics [80, 158],

$$\frac{d}{dt}u_{\text{ex}} = U(1-u_{\text{ex}})\sum \delta(t-t_{\text{ex}}^{\text{spike}}) + \frac{U-u_{\text{ex}}}{\tau_f}, \tag{37}$$

$$\frac{d}{dt}x_{\text{ex}} = -\,u_{\text{ex}}\,x_{\text{ex}}\sum \delta(t-t_{\text{ex}}^{\text{spike}}) + \frac{1-x_{\text{ex}}}{\tau_d}, \tag{38}$$

where u_{ex} is the neurotransmitter release probability, enhanced upon each presynaptic excitatory spike, relaxing to baseline U with time constant τ_f (in ms); x_{ex} is the available synaptic resources after neurotransmitter release, depleted by vesicle pool reduction, recovering with time constant τ_d (in ms); and δ denotes Dirac delta functions at spike times.

To prevent runaway excitation during high postsynaptic firing, we model calcium-dependent spike-frequency adaptation at the postsynaptic end, inspired by mechanisms described in the literature [226, 227]. High postsynaptic spiking elevates intracellular calcium via action potential-triggered activation of voltage-gated calcium channels, leading to adaptation that reduces synaptic responsiveness [226]. In our model, this process attenuates the responsiveness of postsynaptic excitatory and inhibitory neurons through the following dynamics:

$$\frac{d}{dt}y_{\text{post}} = -\eta_y\,\zeta_{\text{post}}\,y_{\text{post}}\sum \delta(t-t_{\text{post}}^{\text{spike}}) + \frac{1-y_{\text{post}}}{\tau_y}, \tag{39}$$

where y_{post} is the postsynaptic adaptation factor, depleted in an activity-dependent manner during spiking and recovering to 1 with time constant τ_y (in ms); η_y (in s^{-1}) is the baseline depletion rate; $\sum \delta(t-t_{\text{post}}^{\text{spike}})$ triggers updates at spike times; and ζ_{post} is the activity-dependent scaling factor, defined as

$$\zeta_{\text{post}} = 1 + \frac{l_\zeta}{1+\exp(-s_\zeta(z_{\text{post}}^{\text{fast}} - k_\zeta))}, \tag{40}$$

with amplitude l_ζ, slope s_ζ, and midpoint threshold k_ζ.

Protein-mediated synaptic stabilization

To capture the stabilization of labile synaptic changes into persistent forms, reflecting synaptic tagging and capture mechanisms [228, 229], we model protein-mediated stabilization of synaptic changes. Long-term synaptic plasticity, such as potentiation (LTP) or depression (LTD), involves early phases (early-LTP or early-LTD) with rapid, labile alterations in receptor density (e.g., AMPA receptor trafficking), but these decay without protein synthesis [83], governed by:

$$\frac{d}{dt}w_{\text{pre}\to\text{post}} = -\frac{w_{\text{pre}\to\text{post}} - \widetilde{w}_{\text{pre}\to\text{post}}}{\tau_w}, \tag{41}$$

where the total synaptic weight, $w_{\text{pre}\to\text{post}}$, decays toward the stable component $\widetilde{w}_{\text{pre}\to\text{post}}$ with τ_w as the decay time constant for labile changes.

Activity-dependent intracellular calcium triggers gene expression and synthesis of plasticity-related proteins (PRPs) through pathways like CaMKK/CaMKIV-CREB [230], which are consumed during stabilization. Thus, we model PRP dynamics as:

$$\frac{d}{dt}\text{PRP}_{\text{post}} = \eta_{\text{prp}}\,\zeta_{\text{post}} \sum \delta(t - t^{\text{spike}}_{\text{post}}) - \frac{\text{PRP}_{\text{post}}}{\tau_{\text{prp}}} - \left|\frac{d}{dt}\widetilde{w}_{\text{pre}\to\text{post}}\right|, \tag{42}$$

where η_{prp} is the baseline PRP increment, τ_{prp} is the PRP decay time constant, and $\left|\frac{d}{dt}\widetilde{w}_{\text{pre}\to\text{post}}\right|$ accounts for PRP consumption proportional to stabilization.

These PRPs are captured by tagged synapses to stabilize labile synaptic changes into late-LTP or late-LTD [228, 231], updating the stable weight, $\widetilde{w}_{\text{pre}\to\text{post}}$, toward $w_{\text{pre}\to\text{post}}$ at a rate scaled by available PRP:

$$\frac{d}{dt}\widetilde{w}_{\text{pre}\to\text{post}} = \frac{\text{PRP}_{\text{post}}}{P} \cdot \frac{w_{\text{pre}\to\text{post}} - \widetilde{w}_{\text{pre}\to\text{post}}}{\tau_{\widetilde{w}}}, \tag{43}$$

where $\tau_{\widetilde{w}}$ is the stabilization time constant and P is the total number of presynaptic neurons.

Network architecture

We develop an entorhinal-hippocampal-cortical network model using Hodgkin-Huxley-type neurons. The model comprises the medial entorhinal cortex (MEC; 16 excitatory, 7 inhibitory neurons), dentate gyrus (DG; 16 excitatory, 7 inhibitory), CA3 (32 excitatory, 9 inhibitory), CA1 (16 excitatory, 8 inhibitory), cortical regions (CR; 16 excitatory, 8 inhibitory), and a background population representing unmodeled areas (240 excitatory, 60 inhibitory).

In non-background regions (MEC, DG, CA3, CA1, CR), excitatory neurons form four cell assemblies per region. Each assembly pairs with one ASIN that delivers feedback inhibition to its own assembly and lateral inhibition to the other three. This reserves four inhibitory neurons per region; they mutually inhibit with a weight of 1 and lack self-inhibition. Remaining inhibitory neurons process feedforward inhibition.

Background neurons are recurrently connected, with each receiving afferents from approximately 48 randomly selected excitatory and 12 randomly selected inhibitory background neurons. Synaptic weights, $w_{\text{pre}\to\text{post}}$, follow a log-normal distribution with parameters $\mu = \ln\left(\frac{\langle w_{\text{pre}\to\text{post}}\rangle^2}{\sqrt{\langle w^2_{\text{pre}\to\text{post}}\rangle}}\right)$ and $\sigma = \sqrt{\ln\left(\frac{\langle w^2_{\text{pre}\to\text{post}}\rangle}{\langle w_{\text{pre}\to\text{post}}\rangle^2}\right)}$ to match specified ensemble averages, where $\langle w_{\text{pre}\to\text{post}}\rangle$ is the mean synaptic weight and $\langle w^2_{\text{pre}\to\text{post}}\rangle$ is the mean squared synaptic weight, fixed for each connection type (E→E, E→I, I→E, I→I), generating asynchronous irregular activity with realistic firing rates [87].

Excitatory neurons in non-background regions receive inputs from approximately 48 random excitatory background neurons, with weights drawn from the same log-normal

distribution. Inhibitory weights for feedforward, feedback, and lateral inhibition depend on corresponding excitatory-to-excitatory updates and are adjusted as described previously. Two inhibitory neurons per non-background region mediate feedforward inhibition from the background.

Inter-regional projections mirror anatomical connectivity [183]: MEC projects to DG, CA3, and CA1 (one inhibitory neuron per target region for feedforward inhibition); DG to CA3 (one in CA3); CA3 to CA1 (one in CA1); and CA1 to CR (one in CR) [232]. Intra-regional recurrent connections are implemented in MEC [233], CA3 [183], and CR [234–236] (one each in MEC, CA3, and CR). Recurrent connectivity in DG and CA1 is not modeled for simplicity, as it is sparse and predominantly inhibitory in nature [79, 237, 238]. MEC→DG/CA3/CA1, CA3→CA1, and CA1→CR projections are performed assemblywise, where a bundle from a cell assembly projects to a respective bundle of a cell assembly in the receiving area in a one-to-one manner [232, 239, 240]. These projections have initial effective synaptic weights (2 for MEC→DG/CA3/CA1 and 6 for CA3→CA1) [241–243] that assist in signal propagation to downstream regions when MEC is stimulated during the encoding phase. In contrast, recurrent connections in MEC, CA3, and CR are all-to-all without self-connections, while DG→CA3 is all-to-all. These connections—critical for sequential engram encoding—have ∼zero initial weights [244], indicating no pre-stored engrams. Before incorporating CA1→CR projections, parameters $g_{\text{pre}\to\text{post}}$ are optimized to yield mean firing rates ($\langle z^1 \rangle$) of ∼1 Hz for background excitatory neurons and ∼6 Hz for inhibitory neurons [87], producing asynchronous-irregular dynamics ($\text{CV}_{\text{ISI}} = 1.03$, $\text{CC} = 0.004$ [245]; excitatory z^1: mean 1.00 Hz, variance 1.03 Hz^2; inhibitory z^1: mean 6.00 Hz, variance 13.96 Hz^2 [87]). Additionally, $w_{\text{inh}\to\text{ex}}$ is tuned for entorhinal, hippocampal, and cortical regions to maintain $\langle z^1 \rangle$ of ∼1 Hz. Subsequently, CA1→CR excitatory projections are added with weight of 2 and accompanied by strong feedforward inhibition inserted with b equals 0.15 [91–94], resisting functional engram maturation in CR before offline consolidation [37].

In the model, inter-regional delays incorporate theta phase progression to create temporal windows for local circuit computations [81, 246, 247]. These delays are set illustratively below empirical upper limits: 15 ms from medial entorhinal cortex (MEC) to dentate gyrus (DG), 20 ms to CA3, and 25 ms to CA1; 15 ms from DG to CA3 and from CA3 to CA1; and 35 ms from CA1 to cortical regions (CR). Intra-regional inter-assembly delays within MEC, CA3, and CR are assumed to be 20 ms to enable sequential activations during offline replays [103, 188, 248, 249]. Intra-assembly delays are 1 ms. Delays from excitatory-to-inhibitory neurons (for feedback/lateral inhibition), from inhibitory-to-excitatory neurons, and from inhibitory-to-inhibitory neurons are 0 ms.

Stimulus-induced theta-phase precession

To simulate the encoding of location sequences, we implement stimulus-induced theta-phase precession in the medial entorhinal cortex (MEC) neurons, mimicking the progressive phase advance of location-specific firing relative to theta oscillations (8 Hz) [250, 251]. Four virtual locations (A–D) are traversed in 1.125 s, spanning nine theta cycles. The 16 MEC excitatory neurons are divided into four cell assemblies (four neurons each), with assemblies 1–4 representing locations A–D, respectively [252, 253].

Stimulation follows a phase-precession pattern across theta cycles:

`|xxxA|xAAx|AAAB|xBBx|BBBC|xCCx|CCCD|xDDx|DDDx|`,

where each segment between vertical bars represents one theta cycle, 'x' denotes no stimulation, and 'A'–'D' indicate stimulation of the corresponding assembly. This pattern replicates the empirical shift of location-tuned firing to earlier theta phases [250]. For repeated explorations of locations A–D, the stimulation pattern is repeated with a gap of one theta cycle following each sequence, such that four complete explorations occur over 40 theta cycles, totaling exactly 5 s.

Each stimulation event consists of a burst of three current pulses with 6-ms inter-pulse intervals, each designed to elicit one spike. For each pulse, external current is applied for up to 2 ms; if a spike occurs sooner, the current is immediately removed to ensure exactly one spike per pulse.

Local field potential proxy estimation

We estimate the proxy for local field potentials (LFPs), $\Phi^R(t)$ (in mV), as proportional to the average post-synaptic current of the excitatory neurons in a region R [254], using a point-source volume conduction approximation [255]:

$$\Phi^R(t) = \frac{\rho_\Phi \; A_\Phi \; N_{\text{ex}}^R}{4\pi r_\Phi} \; \left\langle I_{\text{syn}}^R(t) \right\rangle , \tag{44}$$

where N_{ex}^R is the number of excitatory neurons in R (plus background neurons if R $\neq$ Background), with $R \in \{\text{MEC}, \text{DG}, \text{CA1}, \text{CA3}, \text{CR}, \text{Background}\}$, and $\left\langle I_{\text{syn}}^R(t) \right\rangle$ is their average post-synaptic current density at time t; ρ_Φ (in $\frac{\text{mV}}{\mu A}$cm) is the extracellular resistivity [256, 257], r_Φ (in cm) is the typical electrode distance [255, 258], and A_Φ (in cm^2) is the effective membrane area per neuron, incorporating dendritic contributions based on standard pyramidal cell morphologies [259, 260]. These parameters yield empirically consistent LFP amplitudes [261, 262].

Measures of spike train variability and neuronal synchrony

We quantify the irregularity in neuronal firing patterns using the inter-spike interval coefficient of variation (CV_{ISI}), calculated as

$$\text{CV}_{\text{ISI}} = \left\langle \frac{\sigma_k^{\text{ISI}}}{\mu_k^{\text{ISI}}} \right\rangle , \tag{45}$$

where the angle brackets represent averaging across the entire neuronal population, μ_k^{ISI} denotes the average inter-spike interval for the k-th neuron, and σ_k^{ISI} is its corresponding standard deviation.

To assess the degree of coordinated activity among neurons, we employ the mean pairwise correlation coefficient (CC), defined following [86] by

$$\mathrm{CC} = \left\langle \frac{\mathrm{Cov}(R_m, R_n)}{\sigma(R_m)\sigma(R_n)} \right\rangle, \tag{46}$$

with the averaging performed over every unique pair of neurons. Here, R_m indicates the spike count for neuron m within non-overlapping time bins of 5 ms, $\mathrm{Cov}(R_m, R_n)$ is the covariance between the counts for neurons m and n, and $\sigma(R_m)$ represents the standard deviation of the spike counts for neuron m.

Detection and extraction of sequential cell assembly replays

For each of the four CA1 assemblies, we compute the average synaptic trace across members using a time constant $\tau = 25$ ms ($\langle z^{0.025} \rangle$). Peaks in this trace, corresponding to the maxima of smoothed activation events, are detected to timestamp each assembly activation. To extract sequential replays in the order $1 \to 2 \to 3 \to 4$ (including partial chains of length ≥ 1), we link each peak in assembly k to the nearest subsequent peak in $k+1$ within 125 ms. Longest chains (up to length 4) are constructed first, followed by shorter chains from remaining peaks, with no reuse to avoid overlaps or redundant counts.

Estimation of mean ripple power

Ripple-associated replay power, P_e (in mV^2), in the simulated CA1 LFP time series, Φ, is estimated per replay event as the mean-squared amplitude:

$$P_e = \frac{1}{T_e} \sum_{t=1}^{T_e} \Phi^2(t), \tag{47}$$

where T_e is the number of time points in the replay event. The mean power is then obtained by averaging P_e across replay events.

Numerical Integration

The differential equations were discretized by approximating dt as $\Delta t = 0.025$ ms and dW as $\Delta W \sim \mathcal{N}(0, \Delta t)$. Eq. (1), incorporating stochastic noise, was solved using the stochastic Heun method [263], which provides second-order weak (distributional) convergence and first-order strong (pathwise) convergence. Eqs. (5–7,14–16,20,21) were solved using the deterministic Heun method [264], which provides second-order convergence. Eqs. (27,37–39,41–43) were solved using the forward Euler method [265], which provides first-order convergence.

The values and descriptions of all parameters are provided in Table 1.

Table 1: Parameter values and descriptions

Parameter	Value	Description
Ion concentrations and thresholds		
$K_{i,base}$	140 mM	Equilibrium intracellular K^+ concentration
$Na_{i,ref}$	18 mM	Reference intracellular Na^+ concentration for ion balance
Na_{th}	25 mM	Intracellular Na^+ threshold for half-maximal pump activation
σ_{Na}	3 mM	Steepness of pump response to intracellular Na^+ changes
K_{th}	5.5 mM	Extracellular K^+ threshold for half-maximal pump activation
$[Cl^-]_i$	6 mM	Resting intracellular Cl^- concentration
$[Cl^-]_o$	130 mM	Resting extracellular Cl^- concentration
$[K^+]_{Buffer}$	3.5 mM	Reference extracellular K^+ concentration for buffering
$[Na^+]_{Buffer}$	144 mM	Reference extracellular Na^+ concentration for buffering
Pump activation parameters		
ρ_{max}	1.25 mM/s	Maximum Na^+-K^+ pump transport rate
γ	0.0445 (mM/s)/(μA/cm^2)	Conversion from current density to concentration change
β	7	Intracellular to extracellular volume ratio
ϵ_K	0.33 s^{-1}	Extracellular K^+ clearance rate
Sodium channel kinetics		
$\phi_{\alpha m}$	0.32 ms^{-1}	Scaling factor for Na^+ activation opening rate
$V_{shift,\alpha m}$	54 mV	Voltage shift for Na^+ activation opening midpoint
$\sigma_{\alpha m}$	4 mV	Sensitivity of Na^+ activation opening to voltage changes
$\phi_{\beta m}$	0.28 ms^{-1}	Scaling factor for Na^+ activation closing rate
$V_{shift,\beta m}$	27 mV	Voltage shift for Na^+ activation closing midpoint
$\sigma_{\beta m}$	5 mV	Sensitivity of Na^+ activation closing to voltage changes
Potassium channel kinetics		
$\phi_{\alpha n}$	0.032 ms^{-1}	Scaling factor for K^+ activation opening rate

Table 1: Parameter values and descriptions (continued)

Parameter	Value	Description
$V_{\text{shift},\alpha n}$	52 mV	Voltage shift for K^+ activation opening midpoint
$\sigma_{\alpha n}$	5 mV	Sensitivity of K^+ activation opening to voltage changes
$\phi_{\beta n}$	0.5 ms^{-1}	Scaling factor for K^+ activation closing rate
$V_{\text{shift},\beta n}$	57 mV	Voltage shift for K^+ activation closing midpoint
$\sigma_{\beta n}$	40 mV	Sensitivity of K^+ activation closing to voltage changes
Sodium inactivation kinetics		
$\phi_{\alpha h}$	0.128 ms^{-1}	Scaling factor for Na^+ inactivation onset rate
$V_{\text{shift},\alpha h}$	50 mV	Voltage shift for Na^+ inactivation onset midpoint
$\sigma_{\alpha h}$	18 mV	Sensitivity of Na^+ inactivation onset to voltage changes
$\phi_{\beta h}$	4 ms^{-1}	Scaling factor for Na^+ inactivation recovery rate
$V_{\text{shift},\beta h}$	27 mV	Voltage shift for Na^+ inactivation recovery midpoint
$\sigma_{\beta h}$	5 mV	Sensitivity of Na^+ inactivation recovery to voltage changes
Synaptic and noise parameters		
T_{max}	20 ms^{-1}	Maximum neurotransmitter release rate at synapses
$V_{\text{shift,S}}$	20 mV	Voltage shift for half-maximal synaptic release
σ_{S}	3 mV	Steepness of synaptic release response to presynaptic voltage
τ_{att}	5 ms	Time scale for synaptic attenuation during presynaptic depolarization block
$V_{\text{shift},\chi}$	50 mV	Voltage offset in synaptic attenuation calculation
δ_{χ}	0.4 ms^{-1}	Decay rate for synaptic attenuation fade
η_{max}	0.4 ms^{-1}	Maximum buildup rate for synaptic attenuation
$V_{\text{dep,low}}$	-30 mV	Lower voltage threshold for synaptic attenuation onset

Table 1: Parameter values and descriptions (continued)

Parameter	Value	Description
$V_{\text{dep,high}}$	-10 mV	Upper voltage threshold for synaptic attenuation
σ_{noise}	1.5 mV/$\sqrt{\text{ms}}$	Noise amplitude scaling factor
Membrane conductances and capacitance		
G_{Na}	30 mS/cm^2	Maximum Na^+ channel conductance
G_{K}	25 mS/cm^2	Maximum K^+ channel conductance
G_{NaL}	0.0175 mS/cm^2	Na^+ leak conductance
G_{KL}	0.05 mS/cm^2	K^+ leak conductance
G_{ClL}	0.05 mS/cm^2	Cl leak conductance
G_{ex}	0.022 mS/cm^2	Maximum excitatory synaptic conductance
G_{inh}	0.374 mS/cm^2	Maximum inhibitory synaptic conductance
C	1 μF/cm^2	Membrane capacitance per unit area
Reversal potentials and time constants		
E_{ex}	0 mV	Excitatory synaptic reversal potential
E_{inh}	-80 mV	Inhibitory synaptic reversal potential
τ_{ex}	4 ms	Excitatory synaptic decay time constant
τ_{inh}	8 ms	Inhibitory synaptic decay time constant
Physical constants		
R	8.314 J/molK	Universal gas constant
T	309.15 K	Absolute temperature
F	96485 C/mol	Faraday's constant
Excitatory-to-excitatory long-term plasticity		
A_2^-	7.0×10^{-3}	Pair-based depression amplitude
A_3^-	2.3×10^{-4}	Triplet-based depression amplitude
A_2^+	5.0×10^{-10}	Pair-based potentiation amplitude
A_3^+	6.2×10^{-3}	Triplet-based potentiation amplitude
$\tau_{\text{pre}}^{\text{fast}}$	16.8 ms	Time constant for fast presynaptic trace
$\tau_{\text{post}}^{\text{fast}}$	33.7 ms	Time constant for fast postsynaptic trace
$\tau_{\text{pre}}^{\text{slow}}$	101 ms	Time constant for slow presynaptic trace
$\tau_{\text{post}}^{\text{slow}}$	125 ms	Time constant for slow postsynaptic trace
c_η	16	Scaling factor for firing rate threshold in learning rate
s_η	10	Steepness parameter for learning rate sigmoid

Table 1: Parameter values and descriptions (continued)

Parameter	Value	Description
k_η	0.5	Midpoint threshold for learning rate sigmoid
Inhibitory long-term plasticity		
a	1	Scaling constant for excitatory-to-inhibitory weight updates
b	0.05	Scaling constant for inhibitory-to-excitatory weight updates
c	0.07	Scaling constant for postsynaptic to ASIN weight updates
d	0.0088	Scaling constant for ASIN to self-assembly weight updates
f	0.0352	Scaling constant for ASIN to other-assembly weight updates
l_f^{MEC}	0.1	Minimum scaling value for MEC region
l_f^{DG}	0.4	Minimum scaling value for DG region
l_f^{CA3}	0.3	Minimum scaling value for CA3 region
l_f^{CA1}	0.1	Minimum scaling value for CA1 region
l_f^{CR}	0.3	Minimum scaling value for CR region
$l_f^{\mathrm{Background}}$	0.3	Minimum scaling value for Background region
s_f	25 mM^{-1}	Steepness parameter of the sigmoid for disinhibition factor
k_f	3.275 mM	Midpoint potassium concentration for disinhibition factor
Short-term plasticity		
U	0.2	Baseline neurotransmitter release probability
τ_f	1500 ms	Facilitation time constant for release probability
τ_d	20 ms	Depression time constant for synaptic resource recovery
τ_y	1000 ms	Adaptation recovery time constant
η_y	0.001 s^{-1}	Baseline depletion rate for postsynaptic adaptation
l_ζ	100	Amplitude of the activity-dependent scaling factor
s_ζ	3	Slope of the activity-dependent scaling factor
k_ζ	3	Midpoint threshold of the activity-dependent scaling factor

Table 1: Parameter values and descriptions (continued)

Parameter	Value	Description
Protein-mediated synaptic stabilization		
τ_w	3 h	Decay time constant for labile synaptic changes
$\eta_{\text{prp}}^{\text{exc}}$	6.94×10^{-4}	Baseline PRP increment for excitatory neurons
$\eta_{\text{prp}}^{\text{inh}}$	2.78×10^{-5}	Baseline PRP increment for inhibitory neurons
τ_{prp}	1 h	PRP decay time constant
$\tau_{\widetilde{w}}$	5 min	Stabilization time constant
Network architecture		
$N_{\text{ex}}^{\text{MEC}}$	16	Number of excitatory neurons in MEC
$N_{\text{inh}}^{\text{MEC}}$	7	Number of inhibitory neurons in MEC
$N_{\text{ex}}^{\text{DG}}$	16	Number of excitatory neurons in DG
$N_{\text{inh}}^{\text{DG}}$	7	Number of inhibitory neurons in DG
$N_{\text{ex}}^{\text{CA3}}$	32	Number of excitatory neurons in CA3
$N_{\text{inh}}^{\text{CA3}}$	9	Number of inhibitory neurons in CA3
$N_{\text{ex}}^{\text{CA1}}$	16	Number of excitatory neurons in CA1
$N_{\text{inh}}^{\text{CA1}}$	8	Number of inhibitory neurons in CA1
$N_{\text{ex}}^{\text{CR}}$	16	Number of excitatory neurons in CR
$N_{\text{inh}}^{\text{CR}}$	8	Number of inhibitory neurons in CR
$N_{\text{ex}}^{\text{Background}}$	240	Number of excitatory neurons in Background
$N_{\text{inh}}^{\text{Background}}$	60	Number of inhibitory neurons in Background
$\langle w_{\text{ex}\to\text{ex}} \rangle$	0.37	Mean synaptic weight for E to E connections
$\langle w_{\text{ex}\to\text{ex}}^2 \rangle$	0.30	Mean squared synaptic weight for E to E connections
$\langle w_{\text{inh}\to\text{ex}} \rangle$	0.51	Mean synaptic weight for I to E connections
$\langle w_{\text{inh}\to\text{ex}}^2 \rangle$	0.50	Mean squared synaptic weight for I to E connections
$\langle w_{\text{inh}\to\text{inh}} \rangle$	0.54	Mean synaptic weight for I to I connections
$\langle w_{\text{inh}\to\text{inh}}^2 \rangle$	0.56	Mean squared synaptic weight for I to I connections
$\langle w_{\text{ex}\to\text{inh}} \rangle$	0.68	Mean synaptic weight for E to I connections
$\langle w_{\text{ex}\to\text{inh}}^2 \rangle$	0.70	Mean squared synaptic weight for E to I connections
$D_{\text{MEC}\to\text{DG}}$	15 ms	Delay from MEC to DG
$D_{\text{MEC}\to\text{CA3}}$	20 ms	Delay from MEC to CA3

Table 1: Parameter values and descriptions (continued)

Parameter	Value	Description
$D_{\mathrm{MEC}\to\mathrm{CA1}}$	25 ms	Delay from MEC to CA1
$D_{\mathrm{DG}\to\mathrm{CA3}}$	15 ms	Delay from DG to CA3
$D_{\mathrm{CA3}\to\mathrm{CA1}}$	15 ms	Delay from CA3 to CA1
$D_{\mathrm{CA1}\to\mathrm{CR}}$	35 ms	Delay from CA1 to CR
$D_{\mathrm{inter-assembly}}$	20 ms	Intra-regional inter-assembly delay in MEC, CA3, CR
$D_{\mathrm{intra-assembly}}$	1 ms	Intra-assembly delay
$D_{\mathrm{ex}\to\mathrm{inh}}$	0 ms	Delay from excitatory to inhibitory neurons (feedback/lateral inhibition)
$D_{\mathrm{inh}\to\mathrm{ex}}$	0 ms	Delay from inhibitory to excitatory neurons
$D_{\mathrm{inh}\to\mathrm{inh}}$	0 ms	Delay from inhibitory to inhibitory neurons
Local field potential proxy estimation		
ρ_Φ	0.35 mV/(μA cm)	Extracellular resistivity
r_Φ	0.015 cm	Typical electrode distance
A_Φ	0.0025 cm^2	Effective membrane area per neuron
Numerical integration		
Δt	0.025 ms	Integration time step

References

[1] Müller, G. E. & Pilzecker, A. Experimentelle beiträge zur lehre vom gedächtnis. *Zeitschrift für Psychologie, Ergänzungsband* **1**, 1–300 (1900).

[2] McGaugh, J. L. Memory–a century of consolidation. *Science* **287**, 248–251 (2000).

[3] Sadowski, J. H., Jones, M. W. & Mellor, J. R. Sharp-wave ripples orchestrate the induction of synaptic plasticity during reactivation of place cell firing patterns in the hippocampus. *Cell Reports* **14**, 1916–1929 (2016).

[4] Guskjolen, A. & Cembrowski, M. S. Engram neurons: Encoding, consolidation, retrieval, and forgetting of memory. *Molecular Psychiatry* **28**, 3207–3219 (2023).

[5] Murai, Y. & Goto, A. Diverse synaptic mechanisms underlying learning and memory consolidation. *Current Opinion in Neurobiology* **92**, 102996 (2025).

[6] Bliss, T. V. P. & Collingridge, G. L. A synaptic model of memory: long-term potentiation in the hippocampus. *Nature* **361**, 31–39 (1993).

[7] Malinow, R. & Malenka, R. C. AMPA receptor trafficking and synaptic plasticity. *Annual Review of Neuroscience* **25**, 103–126 (2002).

[8] Swanger, S. A., He, Y. A., Richter, J. D. & Bassell, G. J. Dendritic GluN2A synthesis mediates activity-induced NMDA receptor insertion. *The Journal of Neuroscience* **33**, 8898–8908 (2013).

[9] Mocle, A. J. *et al.* Excitability mediates allocation of pre-configured ensembles to a hippocampal engram supporting contextual conditioned threat in mice. *Neuron* **112**, 1487–1497.e6 (2024).

[10] Uytiepo, M. *et al.* Synaptic architecture of a memory engram in the mouse hippocampus. *Science* **387**, eado8316 (2025).

[11] Frankland, P. W. & Bontempi, B. The organization of recent and remote memories. *Nature Reviews Neuroscience* **6**, 119–130 (2005).

[12] Sun, W., Advani, M., Spruston, N., Saxe, A. & Fitzgerald, J. E. Organizing memories for generalization in complementary learning systems. *Nature Neuroscience* **26**, 1438–1448 (2023).

[13] Chandra, S., Sharma, S., Chaudhuri, R. & Fiete, I. R. Episodic and associative memory from spatial scaffolds in the hippocampus. *Nature* **638**, 739–751 (2025).

[14] Yang, Y., Huang, Z., Yang, Y., Fan, M. & Yin, D. Time-dependent consolidation mechanisms of durable memory in spaced learning. *Communications Biology* **8**, 535 (2025).

[15] Ko, S. Y. *et al.* Systems consolidation reorganizes hippocampal engram circuitry. *Nature* **643**, 735–743 (2025).

[16] Stickgold, R. Sleep-dependent memory consolidation. *Nature* **437**, 1272–1278 (2005).

[17] Clawson, B. C. *et al.* Causal role for sleep-dependent reactivation of learning-activated sensory ensembles for fear memory consolidation. *Nature Communications* **12**, 1200 (2021).

[18] Zhou, Z. & Norimoto, H. Sleep sharp wave ripple and its functions in memory and synaptic plasticity. *Neuroscience Research* **189**, 20–28 (2023).

[19] Staresina, B. P. Coupled sleep rhythms for memory consolidation. *Trends in Cognitive Sciences* **28**, 339–351 (2024).

[20] Ng, T., Noh, E. & Spencer, R. M. C. Does slow oscillation-spindle coupling contribute to sleep-dependent memory consolidation? a bayesian meta-analysis. *eLife* (2024).

[21] Bollmann, L., Baracskay, P., Stella, F. & Csicsvari, J. Sleep stages antagonistically modulate reactivation drift. *Neuron* **113**, 1446–1459.e6 (2025).

[22] Foster, D. J. & Wilson, M. A. Reverse replay of behavioural sequences in hippocampal place cells during the awake state. *Nature* **440**, 680–683 (2006).

[23] Shin, J. D., Tang, W. & Jadhav, S. P. Dynamics of awake hippocampal-prefrontal replay for spatial learning and memory-guided decision making. *Neuron* **104**, 1110–1125.e7 (2019).

[24] Himmer, L., Schönauer, M., Heib, D. P. J., Schabus, M. & Gais, S. Rehearsal initiates systems memory consolidation, sleep makes it last. *Science Advances* **5**, eaav1695 (2019).

[25] Mekbib, D. B. & McDonough, I. M. Reactivation and consolidation of memory traces during post-encoding rest across the adult lifespan. *Annals of Clinical and Translational Neurology* **12**, 246–254 (2025).

[26] Louie, K. & Wilson, M. A. Temporally structured replay of awake hippocampal ensemble activity during rapid eye movement sleep. *Neuron* **29**, 145–156 (2001).

[27] Lee, A. K. & Wilson, M. A. Memory of sequential experience in the hippocampus during slow wave sleep. *Neuron* **36**, 1183–1194 (2002).

[28] Ghandour, K. *et al.* Orchestrated ensemble activities constitute a hippocampal memory engram. *Nature Communications* **10**, 2637 (2019).

[29] Zaki, Y. *et al.* Offline ensemble co-reactivation links memories across days. *Nature* **637**, 145–155 (2025).

[30] Bakermans, J. J. W., Warren, J., Whittington, J. C. R. & Behrens, T. E. J. Constructing future behavior in the hippocampal formation through composition and replay. *Nature Neuroscience* **28**, 1061–1072 (2025).

[31] Mallory, C. S., Widloski, J. & Foster, D. J. The time course and organization of hippocampal replay. *Science* **387**, 541–548 (2025).

[32] Cano, G. & Kempter, R. Conditions for replay of neuronal assemblies. *bioRxiv* 2025.07.08.663644 (2025).

[33] Csicsvari, J. & Dupret, D. Sharp wave/ripple network oscillations and learning-associated hippocampal maps. *Philosophical Transactions of the Royal Society B: Biological Sciences* **369**, 20120528 (2014).

[34] Zhang, J., Ou, J. & Liu, Y. Replay and ripples in humans. *Annual Review of Neuroscience* **48**, 65–84 (2025).

[35] Maviel, T., Durkin, T. P., Menzaghi, F. & Bontempi, B. Sites of neocortical reorganization critical for remote spatial memory. *Science* **305**, 96–99 (2004).

[36] Ji, D. & Wilson, M. A. Coordinated memory replay in the visual cortex and hippocampus during sleep. *Nature Neuroscience* **10**, 100–107 (2007).

[37] Kitamura, T. *et al.* Engrams and circuits crucial for systems consolidation of a memory. *Science* **356**, 73–78 (2017).

[38] Rothschild, G., Eban, E. & Frank, L. M. A cortical-hippocampal-cortical loop of information processing during memory consolidation. *Nature Neuroscience* **20**, 251–259 (2017).

[39] Lensjø, K. K. *et al.* Local inhibitory circuits mediate cortical reactivations and memory consolidation. *Science Advances* **11**, eadu9800 (2025).

[40] Schlingloff, D., Káli, S., Freund, T. F., Hájos, N. & Gulyás, A. I. Mechanisms of sharp wave initiation and ripple generation. *The Journal of Neuroscience* **34**, 11385–11398 (2014).

[41] Buzsáki, G. Hippocampal sharp wave-ripple: A cognitive biomarker for episodic memory and planning. *Hippocampus* **25**, 1073–1088 (2015).

[42] Evangelista, R. *et al.* Generation of sharp wave-ripple events by disinhibition. *The Journal of Neuroscience* **40**, 7811–7836 (2020).

[43] Roux, L., Hu, B., Eichler, R., Stark, E. & Buzsáki, G. Sharp wave ripples during learning stabilize the hippocampal spatial map. *Nature Neuroscience* **20**, 845–853 (2017).

[44] Oliva, A., Fernández-Ruiz, A., Leroy, F. & Siegelbaum, S. A. Hippocampal CA2 sharp-wave ripples reactivate and promote social memory. *Nature* **587**, 264–269 (2020).

[45] Widloski, J. & Foster, D. J. Replay without sharp wave ripples in a spatial memory task. *Nature Communications* **16**, 10287 (2025).

[46] Peyrache, A., Battaglia, F. P. & Destexhe, A. Inhibition recruitment in prefrontal cortex during sleep spindles and gating of hippocampal inputs. *Proceedings of the National Academy of Sciences* **108**, 17207–17212 (2011).

[47] Zhang, C.-L., Sontag, L., Gómez-Ocádiz, R. & Schmidt-Hieber, C. Learning-dependent gating of hippocampal inputs by frontal interneurons. *Proceedings of the National Academy of Sciences* **121**, e2403325121 (2024).

[48] Rezaei, E. & Tohidi, S. Cortical GABAergic inhibition dynamics around hippocampal sharp-wave ripples. *bioRxiv* 2025.08.17.670701 (2025).

[49] Satchell, M. *et al.* Cholinergic modulation of neural networks supports sequential and complementary roles for NREM and REM states in memory consolidation. *PLOS Computational Biology* **21**, e1013097 (2025).

[50] Aime, M. *et al.* Paradoxical somatodendritic decoupling supports cortical plasticity during REM sleep. *Science* **376**, 724–730 (2022).

[51] Wu, K., Han, W. & Lu, W. Sleep and wake cycles dynamically modulate hippocampal inhibitory synaptic plasticity. *PLOS Biology* **20**, e3001812 (2022).

[52] Tamaki, M. *et al.* Complementary contributions of non-REM and REM sleep to visual learning. *Nature Neuroscience* **23**, 1150–1156 (2020).

[53] Takács, V. T. *et al.* Co-transmission of acetylcholine and GABA regulates hippocampal states. *Nature Communications* **9**, 2848 (2018).

[54] Domínguez, S., Fernández de Sevilla, D. & Buño, W. Muscarinic long-term enhancement of tonic and phasic $GABA_A$ inhibition in rat CA1 pyramidal neurons. *Frontiers in Cellular Neuroscience* **10**, 244 (2016).

[55] O'Donnell, J., Zeppenfeld, D., McConnell, E., Pena, S. & Nedergaard, M. Norepinephrine: A neuromodulator that boosts the function of multiple cell types to optimize CNS performance. *Neurochemical Research* **37**, 2496–2512 (2012).

[56] Gais, S. & Born, J. Low acetylcholine during slow-wave sleep is critical for declarative memory consolidation. *Proceedings of the National Academy of Sciences* **101**, 2140–2144 (2004).

[57] Wilson, M. A. & McNaughton, B. L. Reactivation of hippocampal ensemble memories during sleep. *Science* **265**, 676–679 (1994).

[58] Kudrimoti, H. S., Barnes, C. A. & McNaughton, B. L. Reactivation of hippocampal cell assemblies: effects of behavioral state, experience, and EEG dynamics. *Journal of Neuroscience* **19**, 4090–4101 (1999).

[59] Diba, K. & Buzs'aki, G. Forward and reverse hippocampal place-cell sequences during ripples. *Nature Neuroscience* **10**, 1241–1242 (2007).

[60] Ecker, A. *et al.* Hippocampal sharp wave-ripples and the associated sequence replay emerge from structured synaptic interactions in a network model of area CA3. *eLife* **11**, e71850 (2022).

[61] Krause, E. L. & Drugowitsch, J. A large majority of awake hippocampal sharp-wave ripples feature spatial trajectories with momentum. *Neuron* **110**, 722–733.e8 (2022).

[62] Chang, H. *et al.* Sleep microstructure organizes memory replay. *Nature* **637**, 1161–1169 (2025).

[63] Sirota, A., Csicsvari, J., Buhl, D. & Buzsáki, G. Communication between neocortex and hippocampus during sleep in rodents. *Proceedings of the National Academy of Sciences* **100**, 2065–2069 (2003).

[64] Norman, Y. *et al.* Hippocampal sharp-wave ripples linked to visual episodic recollection in humans. *Science* **365**, eaax1030 (2019).

[65] Staresina, B. P., Niediek, J., Borger, V., Surges, R. & Mormann, F. How coupled slow oscillations, spindles and ripples coordinate neuronal processing and communication during human sleep. *Nature Neuroscience* **26**, 1429–1437 (2023).

[66] Robinson, H. L. *et al.* Large sharp-wave ripples promote hippocampo-cortical memory reactivation and consolidation. *bioRxiv* 2025.06.27.662061 (2025).

[67] Girardeau, G., Benchenane, K., Wiener, S. I., Buzsáki, G. & Zugaro, M. B. Selective suppression of hippocampal ripples impairs spatial memory. *Nature Neuroscience* **12**, 1222–1223 (2009).

[68] Jadhav, S. P., Kemere, C., German, P. W. & Frank, L. M. Awake hippocampal sharp-wave ripples support spatial memory. *Science* **336**, 1454–1458 (2012).

[69] van de Ven, G. M., Trouche, S., McNamara, C. G., Allen, K. & Dupret, D. Hippocampal offline reactivation consolidates recently formed cell assembly patterns during sharp wave-ripples. *Neuron* **92**, 968–974 (2016).

[70] Aleman-Zapata, A., Morris, R. G. M. & Genzel, L. Sleep deprivation and hippocampal ripple disruption after one-session learning eliminate memory expression the next day. *Proceedings of the National Academy of Sciences* **119**, e2123424119 (2022).

[71] Ego-Stengel, V. & Wilson, M. A. Disruption of ripple-associated hippocampal activity during rest impairs spatial learning in the rat. *Hippocampus* **20**, 1–10 (2010).

[72] Gridchyn, I., Schoenenberger, P., O'Neill, J. & Csicsvari, J. Assembly-specific disruption of hippocampal replay leads to selective memory deficit. *Neuron* **106**, 291–300.e6 (2020).

[73] Yang, W. *et al.* Selection of experience for memory by hippocampal sharp wave ripples. *Science* **383**, 1478–1483 (2024).

[74] Schapiro, A. C., McDevitt, E. A., Rogers, T. T., Mednick, S. C. & Norman, K. A. Human hippocampal replay during rest prioritizes weakly learned information and predicts memory performance. *Nature Communications* **9**, 3920 (2018).

[75] Huelin Gorriz, M., Takigawa, M. & Bendor, D. The role of experience in prioritizing hippocampal replay. *Nature Communications* **14**, 8157 (2023).

[76] Hodgkin, A. L. & Huxley, A. F. A quantitative description of membrane current and its application to conduction and excitation in nerve. *The Journal of Physiology* **117**, 500–544 (1952).

[77] Pfister, J.-P. & Gerstner, W. Triplets of spikes in a model of spike timing-dependent plasticity. *The Journal of Neuroscience* **26**, 9673–9682 (2006).

[78] House, D. R. C., Elstrott, J., Koh, E., Chung, J. & Feldman, D. E. Parallel regulation of feedforward inhibition and excitation during whisker map plasticity. *Neuron* **72**, 819–831 (2011).

[79] Adaikkan, C. *et al.* Silencing CA1 pyramidal cells output reveals the role of feedback inhibition in hippocampal oscillations. *Nature Communications* **15**, 2190 (2024).

[80] Tsodyks, M. V. & Markram, H. The neural code between neocortical pyramidal neurons depends on neurotransmitter release probability. *Proceedings of the National Academy of Sciences* **94**, 719–723 (1997).

[81] Cutsuridis, V. & Poirazi, P. A computational study on how theta modulated inhibition can account for the long temporal windows in the entorhinal-hippocampal loop. *Neurobiology of Learning and Memory* **120**, 69–83 (2015).

[82] O'Keefe, J. & Recce, M. L. Phase relationship between hippocampal place units and the EEG theta rhythm. *Hippocampus* **3**, 317–330 (1993).

[83] Tsokas, P. *et al.* Local protein synthesis mediates a rapid increase in dendritic elongation factor 1A after induction of late long-term potentiation. *The Journal of Neuroscience* **25**, 5833–5843 (2005).

[84] Shinoda, Y., Tanaka, T., Tominaga-Yoshino, K. & Ogura, A. Persistent synapse loss induced by repetitive LTD in developing rat hippocampal neurons. *PLOS ONE* **5**, e10390 (2010).

[85] Ding, F. *et al.* Changes in the composition of brain interstitial ions control the sleep-wake cycle. *Science* **352**, 550–555 (2016).

[86] Destexhe, A. Self-sustained asynchronous irregular states and updown states in thalamic, cortical and thalamocortical networks of nonlinear integrate-and-fire neurons. *Journal of Computational Neuroscience* **27**, 493–506 (2009).

[87] Mongillo, G., Rumpel, S. & Loewenstein, Y. Inhibitory connectivity defines the realm of excitatory plasticity. *Nature Neuroscience* **21**, 1463–1470 (2018).

[88] Levenstein, D., Buzsáki, G. & Rinzel, J. NREM sleep in the rodent neocortex and hippocampus reflects excitable dynamics. *Nature Communications* **10**, 2478 (2019).

[89] Steriade, M., Nuñez, A. & Amzica, F. A novel slow (< 1 hz) oscillation of neocortical neurons in vivo: depolarizing and hyperpolarizing components. *The Journal of Neuroscience* **13**, 3252–3265 (1993).

[90] Bi, G.-q. & Poo, M.-m. Synaptic modifications in cultured hippocampal neurons: dependence on spike timing, synaptic strength, and postsynaptic cell type. *The Journal of Neuroscience* **18**, 10464–10472 (1998).

[91] Marek, R. *et al.* Hippocampus-driven feed-forward inhibition of the prefrontal cortex mediates relapse of extinguished fear. *Nature Neuroscience* **21**, 384–392 (2018).

[92] Sánchez-Bellot, C., AlSubaie, R., Mishchanchuk, K., Wee, R. W. S. & MacAskill, A. F. Two opposing hippocampus to prefrontal cortex pathways for the control of approach and avoidance behaviour. *Nature Communications* **13**, 339 (2022).

[93] Liu, X., Dimidschstein, J., Fishell, G. & Carter, A. G. Hippocampal inputs engage CCK+ interneurons to mediate endocannabinoid-modulated feed-forward inhibition in the prefrontal cortex. *eLife* **9**, e55267 (2020).

[94] Opalka, A. N., Huang, W.-q., Liu, J., Liang, H. & Wang, D. V. Hippocampal ripple coordinates retrosplenial inhibitory neurons during slow-wave sleep. *Cell Reports* **30**, 432–441.e3 (2020).

[95] Ruggiero, R. N. *et al.* Neuromodulation of hippocampal-prefrontal cortical synaptic plasticity and functional connectivity: Implications for neuropsychiatric disorders. *Frontiers in Cellular Neuroscience* **15**, 732360 (2021).

[96] Chong, Y. S., Ang, S. R. & Sajikumar, S. Beyond boundaries: extended temporal flexibility in synaptic tagging and capture. *Communications Biology* **8**, 553 (2025).

[97] Forli, A., Fan, W., Qi, K. K. & Yartsev, M. M. Replay and representation dynamics in the hippocampus of freely flying bats. *Nature* (2025).

[98] Swanson, R. A. *et al.* Topography of putative bi-directional interaction between hippocampal sharp-wave ripples and neocortical slow oscillations. *Neuron* **113**, 754–768.e9 (2025).

[99] Yamamoto, J. & Tonegawa, S. Direct medial entorhinal cortex input to hippocampal CA1 is crucial for extended quiet awake replay. *Neuron* **96**, 217–227.e4 (2017).

[100] Funane, T. *et al.* Impaired sharp-wave ripple coordination between the medial entorhinal cortex and hippocampal CA1 of knock-in model of Alzheimer's disease. *Frontiers in Systems Neuroscience* **16**, 955178 (2022).

[101] Zutshi, I. & Buzsáki, G. Hippocampal sharp-wave ripples and their spike assembly content are regulated by the medial entorhinal cortex. *Current Biology* **33**, 3648–3659.e4 (2023).

[102] Eliav, T. *et al.* Fragmented replay of very large environments in the hippocampus of bats. *Cell* **188**, 4091–4105.e16 (2025).

[103] Russo, E. & Durstewitz, D. Cell assemblies at multiple time scales with arbitrary lag constellations. *eLife* **6**, e19428 (2017).

[104] Hofer, K. T. *et al.* The hippocampal CA3 region can generate two distinct types of sharp wave-ripple complexes, in vitro. *Hippocampus* **25**, 169–186 (2015).

[105] Oliva, A., Fernández-Ruiz, A., Fermino de Oliveira, E. & Buzsáki, G. Origin of gamma frequency power during hippocampal sharp-wave ripples. *Cell Reports* **25**, 1693–1700.e4 (2018).

[106] Harvey, R. E., Berkowitz, L. E., Savage, D. D. & Clark, B. J. Prenatal alcohol exposure disrupts hippocampal sharp-wave ripple-associated spike dynamics. *bioRxiv* 2021.06.29.450435 (2021).

[107] Li, Z. *et al.* Coordinated NREM sleep oscillations among hippocampal subfields modulate synaptic plasticity in humans. *Communications Biology* **7**, 1236 (2024).

[108] Sakon, J. J. & Kahana, M. J. Hippocampal ripples signal contextually mediated episodic recall. *Proceedings of the National Academy of Sciences* **119**, e2201657119 (2022).

[109] Maslarova, A. *et al.* Spatiotemporal patterns differentiate hippocampal sharp-wave ripples from interictal epileptiform discharges in mice and humans. *bioRxiv* 2025.02.06.636758 (2025).

[110] He, X. *et al.* Abnormal salience network in normal aging and in amnestic mild cognitive impairment and Alzheimer's disease. *Hum Brain Mapp* **35**, 3446–64 (2014).

[111] Jones, E. A., Gillespie, A. K., Yoon, S. Y., Frank, L. M. & Huang, Y. Early hippocampal sharp-wave ripple deficits predict later learning and memory impairments in an Alzheimer's disease mouse model. *Cell Reports* **29**, 2123–2133.e4 (2019).

[112] Cheah, C. S., Lundstrom, B. N., Catterall, W. A. & Oakley, J. C. Impairment of sharp-wave ripples in a murine model of dravet syndrome. *The Journal of Neuroscience* **39**, 9251–9260 (2019).

[113] Zhou, X. *et al.* Disturbance of functional and effective connectivity of the salience network involved in attention deficits in right temporal lobe epilepsy. *Epilepsy & Behavior* **124**, 108308 (2021).

[114] Wiegand, J.-P. L. *et al.* Age is associated with reduced sharp-wave ripple frequency and altered patterns of neuronal variability. *The Journal of Neuroscience* **36**, 5650–5660 (2016).

[115] Noguchi, A., Huszár, R., Morikawa, S., Buzsáki, G. & Ikegaya, Y. Inhibition allocates spikes during hippocampal ripples. *Nature Communications* **13**, 1280 (2022).

[116] Davidson, T. J., Kloosterman, F. & Wilson, M. A. Hippocampal replay of extended experience. *Neuron* **63**, 497–507 (2009).

[117] Fernández-Ruiz, A. *et al.* Long-duration hippocampal sharp wave ripples improve memory. *Science* **364**, 1082–1086 (2019).

[118] Klampfl, S. & Maass, W. Emergence of dynamic memory traces in cortical microcircuit models through STDP. *The Journal of Neuroscience* **33**, 11515–11529 (2013).

[119] Kreiser, R., Aathmani, D., Qiao, N., Indiveri, G. & Sandamirskaya, Y. Organizing sequential memory in a neuromorphic device using dynamic neural fields. *Frontiers in Neuroscience* **12**, 717 (2018).

[120] Pfeiffer, B. E. The content of hippocampal replay. *Hippocampus* **30**, 6–18 (2020).

[121] Asabuki, T. & Fukai, T. Predictive learning rules generate a cortical-like replay of probabilistic sensory experiences. *eLife* **13**, RP92712 (2025).

[122] Suh, J., Foster, D. J., Davoudi, H., Wilson, M. A. & Tonegawa, S. Impaired hippocampal ripple-associated replay in a mouse model of schizophrenia. *Neuron* **80**, 484–493 (2013).

[123] Wang, D. V. & Ikemoto, S. Coordinated interaction between hippocampal sharp-wave ripples and anterior cingulate unit activity. *The Journal of Neuroscience* **36**, 10663–10672 (2016).

[124] Klinzing, J. G., Niethard, N. & Born, J. Mechanisms of systems memory consolidation during sleep. *Nature Neuroscience* **22**, 1598–1610 (2019).

[125] Ngo, H.-V., Fell, J. & Staresina, B. Sleep spindles mediate hippocampal-neocortical coupling during long-duration ripples. *eLife* **9**, e57011 (2020).

[126] Kim, J., Joshi, A., Frank, L. & Ganguly, K. Cortical-hippocampal coupling during manifold exploration in motor cortex. *Nature* **613**, 103–110 (2023).

[127] Goshen, I. *et al.* Dynamics of retrieval strategies for remote memories. *Cell* **147**, 678–689 (2011).

[128] Varela, C. *et al.* Tracking the time-dependent role of the hippocampus in memory recall using DREADDs. *PLOS ONE* **11**, e0154374 (2016).

[129] Akers, K. G. *et al.* Hippocampal neurogenesis regulates forgetting during adulthood and infancy. *Science* **344**, 598–602 (2014).

[130] Epp, J. R., Silva Mera, R., Köhler, S., Josselyn, S. A. & Frankland, P. W. Neurogenesis-mediated forgetting minimizes proactive interference. *Nature Communications* **7**, 10838 (2016).

[131] Richards, B. A. & Frankland, P. W. The persistence and transience of memory. *Neuron* **94**, 1071–1084 (2017).

[132] Hasselmo, M. E. Neuromodulation: acetylcholine and memory consolidation. *Trends in Cognitive Sciences* **3**, 351–359 (1999).

[133] Ohki, T. *et al.* Multivariate sharp-wave ripples in schizophrenia during awake state. *Psychiatry and Clinical Neurosciences* **78**, 507–516 (2024).

[134] Marrosu, F. *et al.* Microdialysis measurement of cortical and hippocampal acetylcholine release during sleep-wake cycle in freely moving cats. *Brain Research* **671**, 329–332 (1995).

[135] Dasari, S. & Gulledge, A. T. M1 and M4 receptors modulate hippocampal pyramidal neurons. *Journal of Neurophysiology* **105**, 779–792 (2011).

[136] Bell, K. A., Delong, R., Goswamee, P. & McQuiston, A. R. The entorhinal cortical alvear pathway differentially excites pyramidal cells and interneuron subtypes in hippocampal CA1. *Cerebral Cortex* **31**, 2382–2401 (2021).

[137] Croce, A., Pelletier, J. G., Tartas, M. & Lacaille, J.-C. Afferent-specific properties of interneuron synapses underlie selective long-term regulation of feedback inhibitory circuits in CA1 hippocampus. *The Journal of Physiology* **588**, 2091–2107 (2010).

[138] Li, K., Koukoutselos, K., Sakaguchi, M. & Ciocchi, S. Distinct ventral hippocampal inhibitory microcircuits regulating anxiety and fear behaviors. *Nature Communications* **15**, 8228 (2024).

[139] Tang, W., Shin, J. D., Frank, L. M. & Jadhav, S. P. Hippocampal-prefrontal reactivation during learning is stronger in awake compared with sleep states. *The Journal of Neuroscience* **37**, 11789–11805 (2017).

[140] Liu, X. & Kuzum, D. Hippocampal-cortical memory trace transfer and reactivation through cell-specific stimulus and spontaneous background noise. *Frontiers in Computational Neuroscience* **13**, 67 (2019).

[141] Buch, E. R., Claudino, L., Quentin, R., Bönstrup, M. & Cohen, L. G. Consolidation of human skill linked to waking hippocampo-neocortical replay. *Cell Reports* **35**, 109193 (2021).

[142] Duan, W. *et al.* Awake reactivation of cortical memory traces predicts subsequent memory retrieval. *Progress in Neurobiology* **250**, 102778 (2025).

[143] Destexhe, A., Rudolph, M. & Paré, D. The high-conductance state of neocortical neurons in vivo. *Nature Reviews Neuroscience* **4**, 739–751 (2003).

[144] Yoshida, K. *et al.* Leak potassium channels regulate sleep duration. *Proceedings of the National Academy of Sciences* **115**, E9459–E9468 (2018).

[145] Dietz, A. G. *et al.* Local extracellular K+ in cortex regulates norepinephrine levels, network state, and behavioral output. *Proceedings of the National Academy of Sciences* **120**, e2305071120 (2023).

[146] Bazhenov, M., Timofeev, I., Steriade, M. & Sejnowski, T. J. Model of thalamocortical slow-wave sleep oscillations and transitions to activated states. *The Journal of Neuroscience* **22**, 8691–8704 (2002).

[147] Funk, C. M. *et al.* Role of somatostatin-positive cortical interneurons in the generation of sleep slow waves. *The Journal of Neuroscience* **37**, 9132–9148 (2017).

[148] Timofeev, I., Grenier, F., Bazhenov, M., Sejnowski, T. J. & Steriade, M. Origin of slow cortical oscillations in deafferented cortical slabs. *Cerebral Cortex* **10**, 1185–1199 (2000).

[149] David, F. *et al.* Essential thalamic contribution to slow waves of natural sleep. *The Journal of Neuroscience* **33**, 19599–19610 (2013).

[150] Holcman, D. & Tsodyks, M. The emergence of up and down states in cortical networks. *PLOS Computational Biology* **2**, e23 (2006).

[151] Frank, M. G. Erasing synapses in sleep: Is it time to be shy? *Neural Plasticity* **2012**, 264378 (2012).

[152] Gleichmann, M., Chow, V. W. & Mattson, M. P. Homeostatic disinhibition in the aging brain and Alzheimer's disease. *Journal of Alzheimer's Disease* **24**, 15–24 (2011).

[153] Issa, N. P., Nunn, K. C., Wu, S., Haider, H. A. & Tao, J. X. Putative roles for homeostatic plasticity in epileptogenesis. *Epilepsia* **64**, 539–552 (2023).

[154] Inan, M., Petros, T. J. & Anderson, S. A. Losing your inhibition: Linking cortical GABAergic interneurons to schizophrenia. *Neurobiology of Disease* **53**, 36–48 (2013).

[155] Liu, X., Kumar, V., Tsai, N.-P. & Auerbach, B. D. Hyperexcitability and homeostasis in Fragile X Syndrome. *Frontiers in Molecular Neuroscience* **14**, 805929 (2022).

[156] Chai, Z., Ma, C. & Jin, X. Homeostatic activity regulation as a mechanism underlying the effect of brain stimulation. *Bioelectronic Medicine* **5**, 16 (2019).

[157] Vogels, T. P., Sprekeler, H., Zenke, F., Clopath, C. & Gerstner, W. Inhibitory plasticity balances excitation and inhibition in sensory pathways and memory networks. *Science* **334**, 1569–1573 (2011).

[158] Zenke, F., Agnes, E. J. & Gerstner, W. Diverse synaptic plasticity mechanisms orchestrated to form and retrieve memories in spiking neural networks. *Nature Communications* **6**, 6922 (2015).

[159] Chen, L., Li, X., Tjia, M. & Thapliyal, S. Homeostatic plasticity and excitation-inhibition balance: The good, the bad, and the ugly. *Current Opinion in Neurobiology* **75**, 102553 (2022).

[160] Tomé, D. F. *et al.* Dynamic and selective engrams emerge with memory consolidation. *Nature Neuroscience* **27**, 561–572 (2024).

[161] Rocchi, L. *et al.* Distinct impacts of sodium channel blockers on the strength-duration properties of human motor cortex neurons. *Epilepsia* (2025).

[162] Tyurikova, O. *et al.* Astrocyte Kir4.1 expression level territorially controls excitatory transmission in the brain. *Cell Reports* **44**, 115299 (2025).

[163] Merolla, A. *et al.* A pH-sensitive closed-loop nanomachine to control hyperexcitability at the single neuron level. *Nature Communications* **15**, 5609 (2024).

[164] Kilman, V., van Rossum, M. C. W. & Turrigiano, G. G. Activity deprivation reduces miniature IPSC amplitude by decreasing the number of postsynaptic $GABA_A$ receptors clustered at neocortical synapses. *The Journal of Neuroscience* **22**, 1328–1337 (2002).

[165] Samokhina, E. *et al.* Potassium homeostasis during disease progression of Alzheimer's disease. *The Journal of Physiology* **603**, 3405–3424 (2025).

[166] Mander, B. A. Local sleep and Alzheimer's disease pathophysiology. *Frontiers in Neuroscience* **14**, 525970 (2020).

[167] Lee, Y. F. *et al.* Optogenetic targeting of astrocytes restores slow brain rhythm function and slows Alzheimer's disease pathology. *Scientific Reports* **13**, 13075 (2023).

[168] Abhyankar, S. D. *et al.* Müller glial Kir4.1 channel dysfunction in *APOE4*-KI model of Alzheimer's disease. *bioRxiv* 2025.02.26.640427 (2025).

[169] Goto, A. *et al.* Stepwise synaptic plasticity events drive the early phase of memory consolidation. *Science* **374**, 857–863 (2021).

[170] Bocchio, M. *et al.* Functional networks of inhibitory neurons orchestrate synchrony in the hippocampus. *PLOS Biology* **22**, e3002837 (2024).

[171] Huang, H. *et al.* Resting-state functional connectivity of salience network in schizophrenia and depression. *Scientific Reports* **12**, 11204 (2022).

[172] Lepeu, G. *et al.* The critical dynamics of hippocampal seizures. *Nature Communications* **15**, 6945 (2024).

[173] Heer, C. M. & Sheffield, M. E. J. Distinct catecholaminergic pathways projecting to hippocampal CA1 transmit contrasting signals during navigation in familiar and novel environments. *eLife* (2024).

[174] Roscow, E. L., Howe, T., Lepora, N. F. & Jones, M. W. Post-learning replay of hippocampal-striatal activity is biased by reward-prediction signals. *bioRxiv* 716290 (2025).

[175] Zheng, J. *et al.* Amygdala-hippocampal dynamics during salient information processing. *Nature Communications* **8**, 14413 (2017).

[176] Bowler, J. C. & Losonczy, A. Direct cortical inputs to hippocampal area CA1 transmit complementary signals for goal-directed navigation. *Neuron* **111**, 4071–4085.e6 (2023).

[177] Issa, J. B., Radvansky, B. A., Xuan, F. & Dombeck, D. A. Lateral entorhinal cortex subpopulations represent experiential epochs surrounding reward. *Nature Neuroscience* **27**, 536–546 (2024).

[178] Robert, V. *et al.* Cortical glutamatergic and GABAergic inputs support learning-driven hippocampal stability. *Science* eadn0623 (2025).

[179] Dabas, A., Bruckner, R., Schultz, H. & Benoit, R. G. Learning from imagined experiences via an endogenous prediction error. *bioRxiv* 2024.06.24.600192 (2024).

[180] Widloski, J. & Foster, D. J. Flexible rerouting of hippocampal replay sequences around changing barriers in the absence of global place field remapping. *Neuron* **110**, 1547–1558.e8 (2022).

[181] Liu, B. & Buonomano, D. V. Ex vivo cortical circuits learn to predict and spontaneously replay temporal patterns. *Nature Communications* **16**, 3179 (2025).

[182] Heckers, S. & Konradi, C. Gabaergic mechanisms of hippocampal hyperactivity in schizophrenia. *Schizophrenia Research* **167**, 4–11 (2015).

[183] van Strien, N. M., Cappaert, N. L. M. & Witter, M. P. The anatomy of memory: an interactive overview of the parahippocampal-hippocampal network. *Nature Reviews Neuroscience* **10**, 272–282 (2009).

[184] Zutshi, I., Valero, M., Fernández-Ruiz, A. & Buzsáki, G. Extrinsic control and intrinsic computation in the hippocampal CA1 circuit. *Neuron* **110**, 658–673.e5 (2022).

[185] Ratigan, H. C., Krishnan, S., Smith, S. & Sheffield, M. E. J. A thalamic-hippocampal CA1 signal for contextual fear memory suppression, extinction, and discrimination. *Nature Communications* **14**, 6758 (2023).

[186] Mölle, M., Yeshenko, O., Marshall, L., Sara, S. J. & Born, J. Hippocampal sharp wave-ripples linked to slow oscillations in rat slow-wave sleep. *Journal of Neurophysiology* **96**, 62–70 (2006).

[187] Prince, T.-M. & Abel, T. The impact of sleep loss on hippocampal function. *Learning & Memory* **20**, 558–569 (2013).

[188] O'Neill, J., Boccara, C. N., Stella, F., Schoenenberger, P. & Csicsvari, J. Superficial layers of the medial entorhinal cortex replay independently of the hippocampus. *Science* **355**, 184–188 (2017).

[189] Schieferstein, N. *et al.* Propagation of sharp wave-ripple activity in the mouse hippocampal CA3 subfield in vitro. *The Journal of Physiology* **602**, 5039–5059 (2024).

[190] Rajasethupathy, P. *et al.* Projections from neocortex mediate top-down control of memory retrieval. *Nature* **526**, 653–659 (2015).

[191] Meier, K., Merseburg, A., Isbrandt, D., Marguet, S. L. & Morellini, F. Dentate gyrus sharp waves, a local field potential correlate of learning in the dentate gyrus of mice. *The Journal of Neuroscience* **40**, 7105–7118 (2020).

[192] Skaggs, W. E., McNaughton, B. L., Wilson, M. A. & Barnes, C. A. Theta phase precession in hippocampal neuronal populations and the compression of temporal sequences. *Hippocampus* **6**, 149–172 (1996).

[193] Stefanini, F. *et al.* A distributed neural code in the dentate gyrus and in CA1. *Neuron* **107**, 703–716.e4 (2020).

[194] Wang, M., Foster, D. J. & Pfeiffer, B. E. Alternating sequences of future and past behavior encoded within hippocampal theta oscillations. *Science* **370**, 247–250 (2020).

[195] D'amour, J. A. & Froemke, R. C. Inhibitory and excitatory spike-timing-dependent plasticity in the auditory cortex. *Neuron* **86**, 514–528 (2015).

[196] Lee, J.-H., Kim, W. B., Park, E. H. & Cho, J.-H. Neocortical synaptic engrams for remote contextual memories. *Nature Neuroscience* **26**, 259–273 (2023).

[197] Panichello, M. F. *et al.* Intermittent rate coding and cue-specific ensembles support working memory. *Nature* **636**, 422–429 (2024).

[198] Kozachkov, L. *et al.* Robust and brain-like working memory through short-term synaptic plasticity. *PLOS Computational Biology* **18**, e1010776 (2022).

[199] Cotton, K. & Ricker, T. J. Examining the relationship between working memory consolidation and long-term consolidation. *Psychonomic Bulletin & Review* **29**, 1625–1648 (2022).

[200] Dragoi, G. & Tonegawa, S. Preplay of future place cell sequences by hippocampal cellular assemblies. *Nature* **469**, 397–401 (2011).

[201] Sharpe, M. J., Batchelor, H. M., Mueller, L. E., Gardner, M. P. H. & Schoenbaum, G. Past experience shapes the neural circuits recruited for future learning. *Nature Neuroscience* **24**, 391–400 (2021).

[202] OLeary, J. D., Bruckner, R., Autore, L. & Ryan, T. J. Natural forgetting reversibly modulates engram expression. *eLife* (2024).

[203] Meltzer, L. A., Yabaluri, R. & Deisseroth, K. A role for circuit homeostasis in adult neurogenesis. *Trends in Neurosciences* **28**, 653–660 (2005).

[204] Lei, B. *et al.* Reconstructing a new hippocampal engram for systems reconsolidation and remote memory updating. *Neuron* **113**, 471–485.e6 (2025).

[205] Golbabaei, A., Coelho, C. A. O., de Snoo, M. L., Josselyn, S. A. & Frankland, P. W. Neurogenesis-dependent transformation of hippocampal memory traces during systems consolidation. *bioRxiv* (2025).

[206] Liao, Z. *et al.* Inhibitory plasticity supports replay generalization in the hippocampus. *Nature Neuroscience* **27**, 1987–1998 (2024).

[207] Tran, L. M. *et al.* Adult neurogenesis acts as a neural regularizer. *Proceedings of the National Academy of Sciences* **119**, e2206704119 (2022).

[208] DeCostanzo, A. J., Fung, C. C. A. & Fukai, T. Hippocampal neurogenesis reduces the dimensionality of sparsely coded representations to enhance memory encoding. *Frontiers in Computational Neuroscience* **12**, 99 (2018).

[209] Goldwyn, J. H. & Shea-Brown, E. The what and where of adding channel noise to the Hodgkin-Huxley equations. *PLOS Computational Biology* **7**, e1002247 (2011).

[210] Faisal, A. A. & Laughlin, S. B. Stochastic simulations on the reliability of action potential propagation in thin axons. *PLOS Computational Biology* **3**, e79 (2007).

[211] Norman, C. A., Krishnakumar, S. S., Timofeeva, Y. & Volynski, K. E. The release of inhibition model reproduces kinetics and plasticity of neurotransmitter release in central synapses. *Communications Biology* **6**, 1091 (2023).

[212] Cressman, J. R., Ullah, G., Ziburkus, J., Schiff, S. J. & Barreto, E. The influence of sodium and potassium dynamics on excitability, seizures, and the stability of persistent states: I. single neuron dynamics. *Journal of Computational Neuroscience* **26**, 159–170 (2009).

[213] Wei, Y., Ullah, G., Ingram, J. & Schiff, S. J. Oxygen and seizure dynamics: II. computational modeling. *Journal of Neurophysiology* **112**, 213–223 (2014).

[214] Destexhe, A., Contreras, D., Sejnowski, T. J. & Steriade, M. A model of spindle rhythmicity in the isolated thalamic reticular nucleus. *Journal of Neurophysiology* **72**, 803–818 (1994).

[215] Destexhe, A., Mainen, Z. & Sejnowski, T. Kinetic models of synaptic transmission. In Koch, C. & Segev, I. (eds.) *Methods in Neuronal Modeling*, chap. 1, 1–25 (MIT Press, Cambridge, 1998), 2 edn.

[216] Ullah, G., Cressman Jr., J. R., Barreto, E. & Schiff, S. J. The influence of sodium and potassium dynamics on excitability, seizures, and the stability of persistent states: II. network and glial dynamics. *Journal of Computational Neuroscience* **26**, 171–183 (2009).

[217] Dutta, S., Iyer, K. K., Vanhatalo, S., Breakspear, M. & Roberts, J. A. Mechanisms underlying pathological cortical bursts during metabolic depletion. *Nature Communications* **14**, 4792 (2023).

[218] Bienenstock, E. L., Cooper, L. N. & Munro, P. W. Theory for the development of neuron selectivity: orientation specificity and binocular interaction in visual cortex. *The Journal of Neuroscience* **2**, 32–48 (1982).

[219] Cooper, L. N. & Bear, M. F. The BCM theory of synapse modification at 30: interaction of theory with experiment. *Nature Reviews Neuroscience* **13**, 798–810 (2012).

[220] Szocs, S., Henn-Mike, N., Agocs-Laboda, A., Szabo-Meleg, E. & Varga, C. Neurogliaform cells mediate feedback inhibition in the medial entorhinal cortex. *Frontiers in Neuroanatomy* **16**, 779390 (2022).

[221] Espinoza, C., Guzman, S. J., Zhang, X. & Jonas, P. Parvalbumin$^+$ interneurons obey unique connectivity rules and establish a powerful lateral-inhibition microcircuit in dentate gyrus. *Nature Communications* **9**, 4605 (2018).

[222] Kriener, B., Chaudhuri, R. & Fiete, I. R. Robust parallel decision-making in neural circuits with nonlinear inhibition. *Proceedings of the National Academy of Sciences* **117**, 25505–25516 (2020).

[223] Rasmussen, R. *et al.* Cortex-wide changes in extracellular potassium ions parallel brain state transitions in awake behaving mice. *Cell Reports* **28**, 1182–1194.e4 (2019).

[224] Brown, R. E., Basheer, R., McKenna, J. T., Strecker, R. E. & McCarley, R. W. Control of sleep and wakefulness. *Physiological Reviews* **92**, 1087–1187 (2012).

[225] Atzori, M. *et al.* Locus ceruleus norepinephrine release: A central regulator of CNS spatio-temporal activation? *Frontiers in Synaptic Neuroscience* **8**, 25 (2016).

[226] Sah, P. Ca^{2+}-activated K^+ currents in neurones: types, physiological roles and modulation. *Trends in Neurosciences* **19**, 150–154 (1996).

[227] Benda, J. & Herz, A. V. M. A universal model for spike-frequency adaptation. *Neural Computation* **15**, 2523–2564 (2003).

[228] Redondo, R. L. & Morris, R. G. M. Making memories last: the synaptic tagging and capture hypothesis. *Nature Reviews Neuroscience* **12**, 17–30 (2011).

[229] Bin Ibrahim, M. Z., Wang, Z. & Sajikumar, S. Synapses tagged, memories kept: synaptic tagging and capture hypothesis in brain health and disease. *Philosophical Transactions of the Royal Society B: Biological Sciences* **379**, 20230237 (2024).

[230] Redondo, R. L. *et al.* Synaptic tagging and capture: Differential role of distinct calcium/calmodulin kinases in protein synthesis-dependent long-term potentiation. *The Journal of Neuroscience* **30**, 4981–4989 (2010).

[231] Clopath, C., Ziegler, L., Vasilaki, E., Büsing, L. & Gerstner, W. Tag-Trigger-Consolidation: A model of early and late long-term-potentiation and depression. *PLOS Computational Biology* **4**, e1000248 (2008).

[232] Cenquizca, L. A. & Swanson, L. W. Spatial organization of direct hippocampal field CA1 axonal projections to the rest of the cerebral cortex. *Brain Research Reviews* **56**, 1–26 (2007).

[233] Zutshi, I. *et al.* Recurrent circuits within medial entorhinal cortex superficial layers support grid cell firing. *Nature Communications* **9**, 3701 (2018).

[234] Mante, V., Sussillo, D., Shenoy, K. V. & Newsome, W. T. Context-dependent computation by recurrent dynamics in prefrontal cortex. *Nature* **503**, 78–84 (2013).

[235] Shahnazian, D. & Holroyd, C. B. Distributed representations of action sequences in anterior cingulate cortex: A recurrent neural network approach. *Psychonomic Bulletin & Review* **25**, 302–321 (2018).

[236] Voigts, J. *et al.* Spatial reasoning via recurrent neural dynamics in mouse retrosplenial cortex. *Nature Neuroscience* **28**, 1293–1299 (2025).

[237] Galloni, A. R., Samadzelkava, A., Hiremath, K., Oumnov, R. & Milstein, A. D. Recurrent excitatory feedback from mossy cells enhances sparsity and pattern separation in the dentate gyrus via indirect feedback inhibition. *Frontiers in Computational Neuroscience* **16**, 826278 (2022).

[238] Engin, E. *et al.* Tonic inhibitory control of dentate gyrus granule cells by α5-containing GABA_A receptors reduces memory interference. *The Journal of Neuroscience* **35**, 13698–13712 (2015).

[239] Dolorfo, C. L. & Amaral, D. G. Entorhinal cortex of the rat: Topographic organization of the cells of origin of the perforant path projection to the dentate gyrus. *Journal of Comparative Neurology* **398**, 25–48 (1998).

[240] Ishizuka, N., Weber, J. & Amaral, D. G. Organization of intrahippocampal projections originating from CA3 pyramidal cells in the rat. *Journal of Comparative Neurology* **295**, 580–623 (1990).

[241] Aguiar, P. d. C. A general hippocampal computational model combining episodic and spatial memory in a spiking model. Ph.D. thesis, University of Edinburgh, College of Science and Engineering, School of Informatics, Edinburgh, UK (2006).

[242] Edvardsen, V. Examining remapping phenomena in a computational model of the hippocampus. Master's thesis, Norwegian University of Science and Technology, Trondheim, Norway (2014).

[243] Wu, Y. & Chen, Z. S. Computational models for state-dependent traveling waves in hippocampal formation. *bioRxiv* 2023.05.19.541436 (2023).

[244] Hopfield, J. J. Neural networks and physical systems with emergent collective computational abilities. *Proceedings of the National Academy of Sciences* **79**, 2554–2558 (1982).

[245] El Boustani, S., Pospischil, M., Rudolph-Lilith, M. & Destexhe, A. Activated cortical states: Experiments, analyses and models. *Journal of Physiology-Paris* **101**, 99–109 (2007).

[246] Mizuseki, K., Sirota, A., Pastalkova, E. & Buzsáki, G. Theta oscillations provide temporal windows for local circuit computation in the entorhinal-hippocampal loop. *Neuron* **64**, 267–280 (2009).

[247] Zielinski, M. C., Shin, J. D. & Jadhav, S. P. Coherent coding of spatial position mediated by theta oscillations in the hippocampus and prefrontal cortex. *The Journal of Neuroscience* **39**, 4550–4565 (2019).

[248] Nádasdy, Z., Hirase, H., Czurkó, A., Csicsvari, J. & Buzsáki, G. Replay and time compression of recurring spike sequences in the hippocampus. *The Journal of Neuroscience* **19**, 9497–9507 (1999).

[249] Liu, Y., Dolan, R. J., Kurth-Nelson, Z. & Behrens, T. E. J. Human replay spontaneously reorganizes experience. *Cell* **178**, 640–652.e14 (2019).

[250] Hafting, T., Fyhn, M., Bonnevie, T., Moser, M.-B. & Moser, E. I. Hippocampus-independent phase precession in entorhinal grid cells. *Nature* **453**, 1248–1252 (2008).

[251] Jeewajee, A. *et al.* Theta phase precession of grid and place cell firing in open environments. *Philosophical Transactions of the Royal Society B: Biological Sciences* **369**, 20120532 (2014).

[252] Harris, K. D., Csicsvari, J., Hirase, H., Dragoi, G. & Buzsáki, G. Organization of cell assemblies in the hippocampus. *Nature* **424**, 552–556 (2003).

[253] Malvache, A., Reichinnek, S., Villette, V., Haimerl, C. & Cossart, R. Awake hippocampal reactivations project onto orthogonal neuronal assemblies. *Science* **353**, 1280–1283 (2016).

[254] Mazzoni, A. *et al.* Computing the local field potential (LFP) from integrate-and-fire network models. *PLOS Computational Biology* **11**, e1004584 (2015).

[255] Lindén, H. *et al.* Modeling the spatial reach of the LFP. *Neuron* **72**, 859–872 (2011).

[256] Ranck, J. B. Specific impedance of rabbit cerebral cortex. *Experimental Neurology* **7**, 144–152 (1963).

[257] Goto, T. *et al.* An evaluation of the conductivity profile in the somatosensory barrel cortex of wistar rats. *Journal of Neurophysiology* **104**, 3388–3412 (2010).

[258] Kajikawa, Y. & Schroeder, C. E. How local is the local field potential? *Neuron* **72**, 847–858 (2011).

[259] Megías, M., Emri, Z., Freund, T. F. & Gulyás, A. I. Total number and distribution of inhibitory and excitatory synapses on hippocampal CA1 pyramidal cells. *Neuroscience* **102**, 527–540 (2001).

[260] Benavides-Piccione, R., Rojo, C., Kastanauskaite, A. & DeFelipe, J. Variation in pyramidal cell morphology across the human anterior temporal lobe. *Cerebral Cortex* **31**, 3592–3609 (2021).

[261] Buzsáki, G., Anastassiou, C. A. & Koch, C. The origin of extracellular fields and currents — EEG, ECoG, LFP and spikes. *Nature Reviews Neuroscience* **13**, 407–420 (2012).

[262] Einevoll, G. T., Kayser, C., Logothetis, N. K. & Panzeri, S. Modelling and analysis of local field potentials for studying the function of cortical circuits. *Nature Reviews Neuroscience* **14**, 770–785 (2013).

[263] Kloeden, P. E. & Platen, E. *Numerical Solution of Stochastic Differential Equations* (Springer, 1992).

[264] Hairer, E., Nørsett, S. P. & Wanner, G. *Solving Ordinary Differential Equations I: Nonstiff Problems* (Springer, 1993).

[265] Butcher, J. C. *Numerical Methods for Ordinary Differential Equations* (John Wiley & Sons, 2016).

Acknowledgments

I am grateful to my immediate and extended family for their selfless, invaluable support.